Pharmacological Interrogation of the *C. elegans* Pharyngeal Cuticle Reveals Small Molecule Amyloid Disruptors

Muntasir Kamal[1,2*], Jessica Knox[1,2*], Duhyun Han[1,2,3], Andrew R. Burns[1,2], Ken CQ Nguyen[4], David H. Hall[4], and Peter J. Roy[1,2,3,5]

1. Department of Molecular Genetics, University of Toronto, Toronto, ON, M5S 1A8, Canada
2. The Donnelly Centre for Cellular and Biomolecular Research, University of Toronto, Toronto, ON, M5S 3E1, Canada
3. Department of Pharmacology and Toxicology, University of Toronto, Toronto, ON, M5S 1A8, Canada
4. Department of Neuroscience, Albert Einstein College of Medicine, New York, New York 10461.

*These authors contributed equally to this work

[5]Corresponding Author: Peter J. Roy
Tel: (416) 946-8395
Fax: (416) 978-6885
E-mail: peter.roy@utoronto.ca

Keywords: *C. elegans*, pharynx, cuticle, pharyngeal cuticle, chitin, chitosan, congo red, thioflavin S, eosin Y, calcofluor white, CFW, EY, intrinsically disordered proteins, IDPs, amyloid, amyloid disruptors, drug screens, chemical biology

Abstract

Understanding how to pharmacologically manipulate amyloids is an essential step towards managing dozens of amyloid-based human diseases. Here, we present a pipeline that yields small molecule antagonists of amyloidogenesis. Screens for small molecules that perturb the development of the nematode *C. elegans* revealed 24 distinct small molecule scaffolds that crystalize on the non-luminal face of the pharyngeal cuticle. Consistent with the amyloid-like nature of the pharyngeal cuticle, 25% of these scaffolds are known to bind human amyloids with nanomolar affinity. The growing crystals preferentially disrupt the amyloid-like material within the cuticle but leave its chitin-based matrix relatively intact. We screened a collection of drugs and natural products for those that suppress crystal formation and found 45 distinct scaffolds, 33% of which are known amyloid busters. Screening for pharmacological suppressors of crystal formation therefore represents an inexpensive high-throughput *in vivo* approach that enriches for small molecules with amyloid-busting potential.

Introduction

Intrinsic disorder within proteins is increasingly recognized as exceptionally useful to biological systems. Intrinsically disordered regions (IDRs) of proteins, or entirely intrinsically disordered proteins (IDPs), can establish multivalent interactions with other IDRs along their unstructured peptide chains (Fung et al., 2018). The amino acid sequence within IDRs often exhibits repeating patterns of physicochemical properties along the protein chain that facilitate interactions with multiple binding partners (Vernon and Forman-Kay, 2019). These properties can include hydrogen bonding capability, π bonding capability, hydrophobicity, and electric charge. By establishing multivalent interactions, IDR-rich proteins can transition from a soluble state into phase-separated states such as liquid condensates (aka liquid-liquid phase separated (LLPS) material), gels, or insoluble amyloid or non-amyloid fibres (Banani et al., 2017). Some examples of intracellular machines that rely on phase-separated material includes germ granules (Brady et al., 2017), P-bodies (Banani et al., 2016) and the nuclear pore complex (Schmidt and Gorlich, 2016). Extracellularly, IDR-rich proteins can self-assemble into a growing list of matrices that include the webs of spiders (Jin and Kaplan, 2003; Slotta et al., 2007), glues secreted by molluscs (Wei et al., 2014b), key elements of the squid beak (Tan et al., 2015), and the recoiling component that surrounds arteries (Muiznieks et al., 2018). The extent to which biology exploits intrinsic disorder is only beginning to be appreciated.

Despite the functionality of intrinsically disordered proteins, their existence carries increased risk to biological systems. IDRs can fall down a well of insolubility wherein

61 phase-separated IDR-rich proteins adopt a kinked β-structure that organizes into
62 insoluble amyloid fibrils (Chiti and Dobson, 2017) or amyloid-like aggregates (McAlary et
63 al., 2019). Over 50 human diseases are linked to amyloid formation (Chiti and Dobson,
64 2017). In some cases, such as Alzheimer's Disease, it remains less clear whether amyloid
65 plaques are causative in the disease (Makin, 2018). In other cases, such as Creutzfeldt-
66 Jakob disease and multiple forms of amyloidosis, amyloid formation is central to disease
67 etiology (see (Chiti and Dobson, 2017) and (Iadanza et al., 2018) for in depth review).
68 Much effort has been devoted to identifying pharmacological agents that directly or
69 indirectly modulate the amyloid state associated with human disease. A few examples
70 of clinically-studied anti-amyloid molecules include doxycycline as a potential treatment
71 for ATTR (transthyretin amyloidosis) (Obici et al., 2012) and AL immunoglobulin light
72 chain amyloidosis (D'Souza et al., 2020; Kumar et al., 2012), CuATSM, which disrupts
73 SOD1 aggregation (Farrawell et al., 2019), is being clinically tested against amyotrophic
74 lateral sclerosis (ALS) (Rowe et al., 2018), and the monoclonal antibody aducanumab,
75 which targets Aβ amyloid (Sevigny et al., 2016) and has been recently been approved by
76 the FDA as a treatment for Alzheimer's in a controversial decision (Mullard, 2021).
77 Despite these examples, there is a paucity of effective treatments for the vast majority
78 of amyloid and aggregation-based human diseases.
79 We have recently generated a spatiotemporal blueprint for the construction of the
80 pharyngeal cuticle of the free-living nematode *Caenorhabditis elegans* (Kamal et al.,
81 Manuscript Submitted). The worm's pharyngeal cuticle is a flexible non-collagenous
82 chitin-rich matrix that is repeatedly shed and rebuilt at each larval stage (Altun and Hall,

83 2020; Cox et al., 1981). The blueprint reveals that successive waves of abundant IDR-rich
84 protein families are likely incorporated into the developing cuticle during the molting
85 period. These IDR-rich proteins are predicted to be capable of phase-separation, and we
86 demonstrated this to be true *in vitro* for an exemplar (Kamal et al., Manuscript
87 Submitted). Computational analyses also indicate that many of these IDR-rich proteins
88 have amyloidogenic features such as an enrichment in π and hydrogen-bonding
89 capability, in addition to having protofilament formation propensity (Kamal et al.,
90 Manuscript Submitted). We speculate that the IDR-rich proteins may form liquid
91 coacervates to fill a chitin matrix during pharyngeal cuticle construction in much the
92 same way that the squid beak is constructed (Tan et al., 2015).
93 Our previous small molecule screens with *C. elegans* revealed many compounds
94 visibly accumulate within the heads of the worm (Burns et al., 2015; Kwok et al., 2006).
95 The accumulation is obvious with the use of a low magnification dissection light
96 microscope and has been observed by other labs (Galford and Jose, 2020; Risi et al.,
97 2019). Depending on the small molecule structure, the accumulated objects form either
98 birefringent irregular objects, globular non-birefringent spheres, or a mixture of the two
99 (Kamal et al., 2019). We previously demonstrated that the birefringent objects: i) are
100 obvious within minutes of exposure of the animal to the small molecule; ii) contain the
101 exogenous small molecule; iii) grow over time; iv) are formed exclusively in association
102 with the pharynx of the worm; and v) are not due to the consumption of precipitate in
103 the media by the worm (Kamal et al., 2019). Given their birefringent nature and their
104 growth over time, we refer to these objects as crystals. The crystals kill younger animals

105 likely because of a combination of factors; they perforate the plasma membrane of
106 surrounding cells and rapidly grow to occlude the pharynx lumen (Kamal et al., 2019).
107 Here, we show that crystal-forming molecules can be grouped into 24 distinct
108 structural scaffolds, six of which have been previously shown to bind amyloid with high
109 affinity. Transmission electron microscopy, pulse-chase experiments and mutant
110 analyses reveal that crystals form in tight association with the non-luminal face of the
111 pharyngeal cuticle. We used multiple dyes and reporters to show that crystal growth
112 disrupts the amyloid-like components of the cuticle without a concomitant effect on the
113 surrounding chitin matrix. A screen of 2558 clinically approved drugs and natural
114 products for those that could suppress crystal formation yielded 45 distinct small
115 molecule scaffolds. 15 (33%) of these have been previously shown to block amyloid
116 formation. Finally, we have identified substructural elements that can convert select
117 small molecule scaffolds from crystal-forming molecules to suppressors of crystal
118 formation and vice-versa, suggesting that crystal-forming molecules and their
119 suppressors likely compete for the same environment within the pharyngeal cuticle. This
120 work reveals the pharyngeal cuticle to be a novel platform with which to identify small
121 molecules that interact with IDR-rich material. We deduce that the complex *in vivo*
122 environment in which these small molecule interactions occur has the potential to
123 reveal novel small molecule modulators of pathogenic amyloid formation.

124 **Results**

125 **64 Small Molecules Induce Crystal Formation in *C. elegans***

126 We previously identified 48 compounds that form crystals in the heads of animals
127 (Kamal et al., 2019). For example, incubating wild type worms in 30 μM of the worm-
128 active #190 small molecule (aka wact-190) for three hours results in obvious crystal
129 formation (Figure 1a-f). More recently, we assembled a distinct custom library of 1178
130 small molecules containing 175 unique core structures that are based upon scaffolds we
131 previously identified as being worm bioactive (Burns et al., 2015) (Supplementary
132 Datafile 1). We screened this library for molecules that kill L1 larvae in our standard 6-
133 day viability assay and identified 88 lethal molecules. We re-screened these lethal hits
134 against the *sms-5(0)* mutant, which we had previously shown to resist crystal-formation
135 (Kamal et al., 2019). We identified 16 molecules that: i) kill wild type; ii) fail to kill *sms-*
136 *5(0)* mutants; and iii) form crystals in association with the pharynx (Figure 1 g and h;
137 Supplemental Figure 1).

138 To investigate the structural diversity among crystal-forming compounds, we created
139 a structural-similarity network by first reducing each molecule to its core scaffold. We
140 then linked the scaffolds that had a Tanimoto similarity coefficient of 0.6 or more (see
141 methods). This produced a network of five clusters that are unconnected with one
142 another and 12 singletons (Figure 1g). Visual inspection reveals 24 distinct structural
143 families that each harbor a distinct core scaffold (Figure 1; Supplemental Figure 1). Nine
144 of these scaffolds contain either an oxadiazole, acetophenone, piperazine, or
145 benzofuran substructure (Figures 1g and 1h; Supplemental Figure 1). In addition to

146 other physicochemical properties that we previously described (Kamal et al., 2019), we
147 found the crystalizing molecules are also enriched in aromatic rings relative to non-
148 crystalizing molecules (*p*=9E-8) (Figure 1i). As discussed below, an enrichment of π
149 bonding capability among the crystalizing compounds (as reflected in their aromaticity)
150 provides insight into why the crystals grow where they do.

151 A search of the patent and academic literature using the SciFinder search tool
152 (Somerville, 1998) revealed that six of the 24 scaffolds are found in molecules that bind
153 amyloid protein. We performed the informatic searches with the core scaffold and not
154 the entire molecule because the small molecule crystallizers are non-drug molecules
155 that have not been widely studied, unlike common drugs and natural products (see
156 below). Scaffolds (a), (b), and the wact-102 scaffold have been shown to bind Abeta42
157 amyloid aggregates with low nanomolar affinity (Watanabe et al., 2009; Yang et al.,
158 2014). Scaffolds (b), (g) and the wact-415 scaffold have been shown to bind prion
159 amyloid aggregates with low nanomolar affinity (Geissen et al., 2011). Finally, wact-498
160 is a flavonoid, which is an intensively studied class of molecules that have therapeutic
161 potential for treating amyloid-related neurodegeneration (reviewed (Ayaz et al., 2019)).
162 In particular, isoflavone analogs of wact-498 can disrupt Abeta42 plaque formation in a
163 *C. elegans* model of the human disease (Gutierrez-Zepeda et al., 2005) and have been
164 shown to directly bind Abeta42 *in vitro* (Hirohata et al., 2012).
165

166 **Crystals Emanate from the Non-Luminal Face of the Pharyngeal Cuticle**

167 For much of our studies of crystal formation, we use either wact-190 as our canonical
168 crystal-forming molecule because it is structurally stable and behaves reproducibly or
169 wact-469 because of its fluorescent properties (Kamal et al., 2019). To better
170 understand the locale of crystal formation, we examined wact-190 objects by
171 transmission electron microscopy (TEM). Through the examination of serial sections, we
172 found that unusual objects form in close association with the non-luminal face of the
173 pharyngeal cuticle (Figures 2a-k). We presume these unusual objects to be the crystals
174 that we see by light microscopy, which also appear to extend from the non-luminal face
175 of the cuticle (see Figure 1f for example). As the objects extend in space, they can be
176 seen either piercing the plasma membrane (Figures 2c, c', i and j) or adjacent to the
177 plasma membrane like a finger pushing on the skin of a balloon (Figures 2f,f'). In either
178 case, the extension of the object from the pharyngeal cuticle is coincident with the
179 distortion of the plasma membrane inwards towards the cytoplasm.

180 We note the irregular amorphous material in the space between the objects and the
181 plasma membrane that are routinely observed in the experimental samples (e.g., pink
182 arrowhead in Figure 2h). This material is remarkably similar to that which forms
183 between the old cuticle that separates from the newly synthesized cuticle during
184 apolysis (for example, see Figure 8 of (Wright and Thomson, 1981)). This suggests that
185 the debris may be a consequence of disrupted cuticle.

186 The larval stages of *C. elegans* are defined by cuticle molts where the animal sheds its
187 old cuticle and grows a new one underneath (Knight et al., 2002). If we are correct in our

188 interpretation that objects form in association with the pharyngeal cuticle, then
189 removing larval worms from a solution of the object-forming compound should result in
190 the shedding of the crystals along with the old cuticle during the subsequent molt. If
191 instead the crystals initially form within the plasma membrane or in the cytoplasm, then
192 the crystals should remain after the molt. We used an established pulse-chase protocol
193 to determine whether the crystals were likely associated with the pharyngeal cuticle
194 (Figure 2l; see methods for details) (Kamal et al., Manuscript Submitted). Briefly, we
195 incubated third larval stage (L3) animals with a pulse of the fluorescent crystalizing
196 molecule wact-469 for three hours, transferred the animals to a rinse plate, and then a
197 chase plate without wact-469. We counted the number of animals with and without
198 fluorescent signal at the beginning and then at the end of the 18 hour chase (Figure 2l).
199 After the chase, very few animals that were initially L3s had fluorescent signal (Figure
200 2m-o). By contrast, when the pulse-chase experiment was done with young adults,
201 which do not molt, the fluorescent signal persisted (Figure 2p-r).
202 We investigated the site of crystal formation using a third approach. Previous work
203 showed that RNAi targeting *mlt-9* results in animals that remain attached to their shed
204 anterior exocuticle and pharyngeal cuticle (Frand et al., 2005; Kamal et al., Manuscript
205 Submitted). We investigated whether attached shed pharyngeal cuticle would
206 accumulate fluorescent crystals when incubated in wact-469 for 3 hours and found that
207 it did (Figure 2s-t). Together, these data indicate that wact-190 birefringent crystals
208 form in tight association with the non-luminal face of the pharyngeal cuticle and can
209 distort the plasma membrane of cells that line the pharynx lumen (Figures 2u-x).

210 **Crystals Disrupt the Amyloid-Like Material of the Pharyngeal Cuticle**

211 We sought to better understand how crystal growth perturbs the materials of the
212 cuticle. To investigate, we used cuticle-binding dyes and fluorescent reporters. We
213 previously found that the red fluorescent Congo Red (CR) and blue fluorescent
214 Thioflavin S (ThS), both of which are well-established amyloid binders (Bennhold, 1922;
215 Divry, 1927; Larbig et al., 2007; Vassar and Culling, 1959), specifically bind the
216 pharyngeal cuticle (Kamal et al., Manuscript Submitted). Similarly, the blue fluorescent
217 Calcofluor white (CFW) and the yellow-red fluorescent Eosin Y (EY), which bind chitin
218 (Harrington and Raper, 1968) and its deacetylated derivative chitosan (Baker et al.,
219 2007) respectively, specifically bind the pharyngeal cuticle (Kamal et al., Manuscript
220 Submitted).

221 We incubated worms in wact-190 and wact-390 (a second crystalizing molecule) for
222 three hours followed by 2 hours of incubation of the dyes (see methods). We found that
223 the amyloid dye patterns are often disrupted by the nascent objects (Figure 3). We also
224 observe a similar pattern in the background where a single IDR-rich protein (ABU-14) is
225 tagged with GFP (George-Raizen et al., 2014) (Supplemental Figure 2). By contrast, the
226 chitin and chitosan dyes are relatively unperturbed (Figure 3; Supplemental Figure 2). In
227 some instances, the birefringent crystal overlaps with amyloid stain (blue arrows, Figure
228 3). In other cases, there is little overlap between the birefringent signal and the amyloid
229 stain (orange arrows, Figure 3).

230 To control for the possibility that the dyes bind the crystals, we asked whether the
231 dyes bind to *in vitro* precipitated small molecules (see methods). None of the dyes

232 fluoresced brightly in association with the *in vitro* precipitated small molecules (Figure
233 3g). We also examined the dye-staining patterns in the presence of much larger 24 hour
234 old *in vivo* crystals. We found many obvious examples where the larger birefringent
235 signals do not overlap with the CR signal (orange arrows, Supplemental Figure 3). These
236 results suggest that nascent crystals can displace the CR-stained material, which often
237 appears to surround the small crystals. This is consistent with the matrix-like material
238 that surrounds the objects in the TEM images (e.g. Figure 2h). As the crystals grow, their
239 larger mass becomes more distinct from the cuticle and their intimate association with
240 the amyloid-staining material is often lost.
241
242 **Crystal Formation is Suppressed by Canonical Amyloid Dyes and Disruptors**
243 To better understand the interaction between crystals and the pharyngeal cuticle, we
244 screened Microsource's Spectrum library of 2558 drugs and natural products for those
245 that might suppress crystal formation. We reasoned that suppressors of crystal
246 formation with common mechanisms of action might lead to insight into crystal
247 formation.
248 We screened the Spectrum library in our standard six-day liquid viability assay
249 whereby multi-well plates are seeded with first larval stage animals (see methods and
250 (Burns et al., 2015)). We previously established wact-190's lethality in young larvae is
251 dependent on crystal formation (Kamal et al., 2019). Control (solvent-only) wells are
252 overgrown with worms after six days (Supplementary Table 1). By contrast, wells with

253 wact-190 (3.75 μM) contain either arrested or dead L1s at the assay endpoint
254 (Supplementary Table 1 and (Kamal et al., 2019)).
255 Screening the Spectrum library molecules at 60 μM yielded 85 hits that: i) suppress
256 wact-190-induced lethality; ii) suppress wact-190 crystal formation ($p<0.05$); and iii) fail
257 to suppress lethality induced by a counter-screen control that does not form crystals
258 (the succinate dehydrogenase inhibitor wact-11 (Burns et al., 2015)) (Supplementary
259 Table 1). To assess the structural diversity of the suppressors, we built a structural
260 similarity network of the molecules (Figure 4a). A Tanimoto coefficient cut-off of 0.8
261 revealed 45 distinct core scaffolds, 18 of which are represented by multiple molecules
262 (Figure 4a-b).
263 Informatic analyses of the 85 suppressors revealed that 15 of the 45 scaffold groups
264 (33%) contained at least one molecule known to play a direct role in disrupting amyloid
265 fibril formation (bold outline in Figure 4a; Supplementary Table 1). The majority of these
266 scaffolds are enriched among the suppressors relative to the entire Spectrum library
267 (see Figure 4b for *p* values). A benzaldehyde substructure is significantly enriched
268 among the suppressors (2.8 fold enrichment, p=2.3E-14; blue highlight in Figure 4b). Of
269 note, we found that several of the suppressors are fluorescent and of these, all
270 specifically stain the pharyngeal cuticle (Figure 4c and Supplemental Figure 4).
271 We investigated whether the set of 85 wact-190 suppressors is enriched for amyloid
272 disruptors relative to the molecules within the Spectrum library. The lack of a
273 comprehensive database of previously characterized small molecule amyloid disruptors
274 precluded a systematic analysis of amyloid disruptors within the Spectrum library. We

275 therefore randomly selected 100 molecules from the remaining 2473 Spectrum library
276 molecules to further investigate. We used the same analytical approach that we
277 employed for the 85 Spectrum suppressors. We first assembled the random molecules
278 into a structural similarity network, revealing 75 structurally-distinct scaffolds (11
279 clusters plus 64 singletons) (Supplemental Figure 5a). We then investigated the
280 literature for evidence of the ability to disrupt amyloid fibril formation for each of the
281 100 random molecules (see methods). Two of the 75 core scaffolds (3%) had one
282 molecule shown to be a disruptor of amyloid fibril formation (Supplemental Figure 5b).
283 From this limited analysis, we find that the 85 Spectrum suppressors are over 10-fold
284 enriched in amyloid disruptors relative to the randomly selected set.
285 We further explored the idea that amyloid interactors might suppress crystal
286 formation. First, we asked whether wact-190-associated lethality is suppressed by the
287 canonical amyloid-binding dyes CR and ThS, neither of which are present in the
288 Spectrum library. Indeed, we found that CR and ThS robustly suppresses wact-190
289 lethality whereas the chitin/chitosan-binding dyes do not (Figure 5a). Second, we asked
290 whether the canonical amyloid-binding dyes can suppress wact-190 crystal formation.
291 We incubated CR and ThS, along with CFW and EY with the animals either for 3 hours
292 before incubating the worms with wact-190 for 3 hours (i.e. a pre-incubation) or at the
293 same time as a 3 hour incubation with wact-190 (i.e. a co-incubation). We found that
294 both CR and ThS suppress crystal formation in both incubation schemes, but that the
295 CFW and EY dyes do not (Figure 5b and 5c). Together, the data suggests that amyloid-

296 binding molecules may outcompete crystalizing molecules for interaction with the
297 pharyngeal cuticle.
298
299 **A Scaffold's Ability to Crystalize or Suppress Crystallization is Interchangeable**
300 Inspection of the structures of crystallizers and suppressors revealed that the former
301 have obviously fewer hydrogen-bond donors than the latter and completely lacked
302 hydroxyl groups (p<1E-10) (Figure 6a-b). The crystallizers are also more halogenated
303 than the suppressors (Figure 6c). We also found that some crystallizers share the
304 identical scaffold as some suppressors. For example, the scaffolds of the wact-128 and
305 wact-498 crystallizers are identical to that of oxyclozanide and koparin crystal
306 suppressors, respectively (Figure 6d). In addition, the wact-415 crystalizing scaffold is
307 similar to that of ThS, which also suppresses crystal formation (Figure 6d). These
308 observations raised the possibility that both classes of molecules (crystallizers and
309 suppressors) compete for the same environment within the cuticle, which would be
310 consistent with their localization to that structure.
311 We tested whether we could convert a crystalizing molecule into a suppressor, and a
312 suppressor into a crystallizer, by altering the abundance of hydroxyl and halogen
313 decorations on the respective core structures. To do this, we searched the ZINC
314 database of the world's commercially available molecules (Sterling and Irwin, 2015) for
315 close structural analogs of the 85 suppressors that lacked hydroxyl groups and are
316 halogenated. We screened 33 available analogs of 6 different suppressors. We found
317 that 11 (33%) of these molecules induced object formation within the pharynx in at least

318 25% of the population (Supplemental Table 2; Figure 6e). This is comparable to the 36%
319 of molecules that induce object formation from our heavily biased collection of worm
320 bioactive small molecules (Kamal et al., 2019). Second, we tested 25 hydroxylated
321 analogs of 10 different crystalizing small molecules for their ability to suppress the
322 lethality associated with crystal-forming wact-190. Five of the 25 hydroxylated
323 crystallizers (20%) suppress wact-190 lethality, and all of these suppress wact-190
324 crystal formation ($p<0.05$) (Supplemental Table 3; Figure 6f). We conclude that select
325 core small molecule structures can be pushed towards crystal formation or its
326 suppression by changing the relative abundance of halogens and hydroxyls that
327 decorate the molecule. Furthermore, the data further supports the model that
328 crystallizers and suppressors likely compete for the same niche.

329 **Discussion**

330 Crystal accumulation within the heads of *C. elegans* is commonly observed in small
331 molecule screens and assays. Here, we investigated this phenomenon in detail and show
332 that: i) many crystal-forming molecules have a core scaffold known to bind amyloid; ii)
333 crystals grow on the non-luminal face of the pharyngeal cuticle; iii) crystals can displace
334 amyloid dye-binding material within the pharyngeal cuticle; and iv) crystal formation is
335 antagonized by small molecules known to interact with amyloid material. We have
336 shown in companion work that the pharyngeal cuticle is rich in proteins with intrinsically
337 disordered regions (IDRs) with both phase-separation and amyloidogenic potential
338 (Kamal et al., Manuscript Submitted). Together, the data suggests that these small
339 molecule interactions occur in an environment abundant with amyloid-like material.

340 Despite being associated with IDR-rich proteins, IDR-rich material is not sufficient for
341 crystal growth. For example, the hypodermis that makes the body cuticle secretes
342 abundant intrinsically disordered proteins with amyloidogenic potential (see Figure 6 of
343 (Kamal et al., Manuscript Submitted)), yet crystal formation is restricted to the
344 pharyngeal cuticle. Similarly, the eggshell is rich in chitin (Zhang et al., 2005), but does
345 not develop birefringent crystals (see Supplemental Figure 3 in (Kamal et al., 2019)).
346 Hence, the niche in which crystals grow is complex and likely requires more than just
347 amyloid-like material and chitin.

348 The physicochemical properties of the small molecules that crystalize provide insight
349 into why these molecules may accumulate specifically within the pharyngeal cuticle.
350 Relative to the non-crystal-forming compounds tested, the crystal-forming compounds

351 are rich with π bonding capability, hydrogen bond acceptors, and polar surface areas
352 (this work and (Kamal et al., 2019)). Our companion analyses show that the pharyngeal
353 secretome is highly enriched in π-bonding capability relative to the remaining proteome
354 and is only surpassed by one other group of proteins (the collagens) (Kamal et al.,
355 Manuscript Submitted). What further distinguishes the pharynx secretome relative to all
356 other protein groups is that its proteins are enriched in polar uncharged residues with
357 hydrogen bond donor capability (i.e., Ns, Qs, Ss, Ts, and Ys) ((p<1E-11) (Kamal et al.,
358 Manuscript Submitted)). Hence, there is unique complementarity between the crystal-
359 forming compounds and their niche within the pharyngeal cuticle.

360 Our finding that select crystallizing molecules and their respective suppressors have
361 identical core structures was unexpected. This suggests that both classes of molecules
362 compete for the same niche. We speculate that the suppressors' enrichment of
363 hydrogen bonding capability (relative to the crystallizers) may facilitate additional
364 interactions with the niche. In turn, the suppressors might prophylactically mask the
365 niche to prevent crystal seeding. This finding also suggests that it might be possible to
366 convert any crystallizing molecule into a suppressor by generating analogs with
367 hydrogen bond-donor capability. Given that a large fraction of suppressors antagonize
368 amyloid formation, converting crystalizing molecules to suppressors represents an
369 additional route towards identifying novel anti-amyloid agents.

370 Many crystal suppressors are known antagonists of amyloid formation. For example,
371 the heme and chlorophyl precursor protoporphyrin IX, its synthetic derivative
372 haematoporphyrin, and chlorophyllide-Cu are the only porphyrins contained within the

373 Spectrum library and all three were found to suppress crystal formation. Multiple
374 studies have shown that porphyrins suppress amyloid formation both *in vivo* and *in vitro*
375 and act through direct interaction with amyloidogenic proteins (Caughey et al., 1998;
376 Lee et al., 2015; Yuan and Gao, 2013). The porphyrins ring is thought to disrupt the
377 intrapeptide π-π interactions of the amyloidogenic peptide that is necessary to achieve
378 superstructure (Yuan and Gao, 2013). Given that the crystalizing molecules are rich in π
379 bonding capability, it may be that porphyrins suppress crystal formation by disrupting
380 the crystallizing molecule's ability to establish π bonds with other molecules of the same
381 type.

382 A second common suppressor class are the flavonoids, which are a large class of
383 polyphenolic secondary metabolites synthesized by plants (Panche et al., 2016). Many
384 flavonoid structures have been shown to antagonize amyloid formation *in vitro* (Akaishi
385 et al., 2008; Choi et al., 2020; Yin et al., 2011), in culture (Kimura et al., 2018), and *in*
386 *vivo* (Ahmad et al., 2017; Kim et al., 2010; Wei et al., 2014a) (see (Hole and Williams,
387 2021) for a comprehensive and recent review). Poor bioavailability may contribute to a
388 lack of flavonoid-based therapies in the clinic, although converting anti-amyloid
389 flavonoids into prodrugs may circumvent absorption barriers (Chen et al., 2018).
390 Flavonoid interaction with Abeta42 is driven by hydrophobic and hydrogen bond
391 interactions that antagonize the peptide's ability to adopt a β-sheet secondary structure
392 (Wang et al., 2015). Whether the flavonoids interact with amyloidogenic proteins within
393 the cuticle in a similar way to suppress crystallization remains to be determined.

394 A third of the suppressor scaffolds are proven amyloid disruptors, suggesting that
395 other molecules within the collection might also disrupt amyloids. It will be a future
396 priority to determine whether the collection contains novel scaffolds that can disrupt
397 disease-related amyloids. Notably, screens for suppressors of the crystal-induced death
398 of *C. elegans* is inexpensive and adaptable to high throughput methodologies.
399 Furthermore, the *in vivo* environment in which suppressors must act is complex and,
400 relative to other *in vitro* assays, may better approximate the environment in which anti-
401 amyloid drugs must act. Crystal suppression therefore represents a novel approach to
402 reveal new candidate amyloid disruptors.
403

404 **Methods**

405 ***C. elegans* Culture, Strains and Microscopy**

406 *C. elegans* strains were cultured and synchronized as previously described (Kamal et al.,
407 2019). Six day viability assays were conducted as previously described (Burns et al.,
408 2015). The wild type N2 Bristol strain was used (obtained from the *C. elegans* genetic
409 Centre); NQ824 qnEx443[Pabu-14:abu-14:sfGFP; rol-6(d); unc-119(+)], which was a kind
410 gift from David Raizen (George-Raizen et al., 2014), was integrated into the genome in
411 our lab as *trIs113*. For all imaging, a Leica DMRA compound microscope with a Qimaging
412 Retiga 1300 monochrome camera was used. Before mounting worms on a 3% agarose
413 pad for imaging, worms are washed 3X with M9 buffer and paralyzed with 50 mM
414 levamisole or 30 mM NaN_3. Transmission electron microscopic (TEM) analysis was
415 performed as previously described (Kamal et al., 2019).

416

417 **Identification of New Crystallizing Molecules and Crystal Counts**

418 A library of 1178 commercially available analogs of *C. elegans*-lethal molecules from the
419 previously reported worm-active (aka wactive) library (Burns et al., 2015) was
420 assembled and purchased from ChemBridge (Supplemental Data File 1). This library was
421 screened at 30 µM in liquid NGM media against synchronized *C. elegans* L1 larvae and
422 *Rhabditophanes diutinus* (Dulovic et al., 2020) as previously described (Burns et al.,
423 2015), with approximately 20 L1s plated per well of a 96-well plate. The final volume in
424 each well was 100 µL and the DMSO concentration was 0.3% v/v. After 6 days of
425 incubation at 25°C the number of living worms in each well was quantified. Molecules

426 that killed *C. elegans* N2 and ***Rhabditophanes*** were tested for resistance in *C. elegans*
427 *sms-5(ok2498)* mutants at 1.9, 7.5, and 30 μM. Crystal counts were performed as
428 previously described (Kamal et al., 2019).
429
430 **Identification of Chemical Suppressors of Crystal-Induced Death and Crystal Formation**
431 To identify chemical suppressors of crystal-induced death, the Spectrum Collection
432 (MicroSource Discovery Systems Inc.) comprised of 2560 approved drugs and natural
433 products was screened at a concentration of 60 μM in the background of 3.75 μM wact-
434 190. This concentration of wact-190 results in crystal formation in the pharynx causing
435 *C. elegans* N2 to arrest at the L1 stage. This screen was performed in liquid NGM media
436 as previously described (Burns et al., 2015), with approximately 20 N2 L1s plated per
437 well of a 96-well plate. The final volume in each well was 50 μL and the DMSO
438 concentration was 0.8% v/v. After 6 days of incubation at 20°C the number adult and
439 larval worms that have progressed from arrested L1 stage was quantified. Hits that
440 suppressed the wact-190 crystal-induced L1 arrest were retested against solvent
441 control, wact-190, and the non-crystal forming lethal molecule wact-11 [10 μM] (see
442 (Burns et al., 2015)) using the same method described above. Hits were further
443 investigated for their ability to suppress crystal formation by co-incubating 3.75 μM of
444 wact-190 and 60 μM of the suppressor with wild type animals in 96 well plate format.
445 The fraction of animals with birefringent crystals was then counted at 100X
446 magnification 48 hours later, counting 20 animals per sample per trial on average.
447

448 **Chemoinformatic Network Analysis, Network Display, Small Molecule Art, and**
449 **Informatic Analyses**

450 Structural similarity networks were constructed based on pairwise similarity scores
451 calculated as the Tanimoto coefficient of shared FP2 fingerprints. Pairwise similarity
452 scores were calculated using OpenBabel (http://openbabel.org) and the networks were
453 visualized using Cytoscape (Cline et al., 2007) as previously described (Burns et al.,
454 2015). For each network generated, a range of Tanimoto coefficient cut-offs were tested
455 to determine which cut-off yielded a network that clustered obvious structural analogs
456 together as determined by manual inspection. Suppressors were analysed for the
457 presence of substructures (Figure 4b) using Filter-it version 1.0.2 from Silicos-it.
458 Structures were drawn using ChemDraw (PerkinElmer Informatics). A random Spectrum
459 network (Supplemental Figure 5) was generated by assigning all molecules within the
460 Spectrum library a random number using excel, then sorting the molecules in order of
461 the random number, then choosing the top 100 molecules that did not include any of
462 the 85 Spectrum suppressors.

463 We analyzed both the list of 85 Spectrum suppressors of crystal formation and the
464 100 randomly chosen molecules by searching that compound and the word 'amyloid' in
465 both a pubmed search and a google search. We inspected the search results for
466 evidence that the molecule of interest had a demonstratable inhibitory effect on
467 amyloid formation *in vitro*, with or without supporting *in vivo* evidence. *In vivo* or *in*
468 *silico* evidence of a decrease in fibril abundance without evidence of a direct effect was
469 excluded from consideration. Molecules that lacked evidence for a direct effect, but had

470 close structural analogs that have a demonstratable inhibitory effect on fibral formation
471 were also excluded from further consideration.
472 To identify hydroxylated analogs of the crystallizing molecules and reduced analogs of
473 the suppressors, Open Babel (O'Boyle et al., 2011) was used for the analog searches.
474 Using SmiLib v2.0 (Schüller et al., 2007), a virtual library of approximately 55,000
475 variably hydroxylated analogs of 161 distinct crystallizing molecules was generated, as
476 well as a virtual library of approximately 950,000 de-hydroxylated and variably
477 halogenated analogs of 12 distinct crystal suppressor molecules. The 55K and 950K
478 virtual libraries were de-duplicated and independently combined with de-duplicated
479 and de-salted versions of MolPort's All Stock Compounds Database and the ZINC In-
480 Stock Database (Sterling and Irwin, 2015). A duplicate search of these combined
481 datasets revealed 34 crystallizer analogs and 88 crystal suppressor analogs that were
482 available for purchase from MolPort. These analogs were further filtered by price, real
483 availability, redundancy among parent Spectrum suppressors, and aqueous solubility,
484 leaving 26 crystallizer analogs and 33 crystal suppressor analogs to be assayed.
485
486 **Pulse Chase Analyses**
487 Pulse chase experiments were performed as previously described (Kamal et al.,
488 Manuscript Submitted). Briefly, synchronized 'L3' or 'adult' were washed with M9 to
489 remove bacteria. Worms were transferred using siliconized tips with the ends cut with
490 flame-sterilized scissors to avoid injuring the worms. 50 μL of packed worms from
491 centrifugation were used per sample, ensuring that the number of worms did not

492 exceed 1000 because the number of worms can affect stain intensity. The tubes with
493 worms and dye, wactive, or control, were incubated on a nutator for 3 hours in the dark
494 at room temperature, rinsed several times, then spotted onto the clear (agar) surface of
495 6 cm plates seeded with OP50. 30 minutes later, 20-30 worms were picked onto a
496 second plate lightly seeded with OP50. The staining of the cuticle for each was then
497 semi-quantitatively assessed on an epifluorescent microscope. These data represent the
498 pre-chase counts. The remaining animals on the original 6 cm plate are incubated for a
499 total of 18 hours at 20°C, after which dye staining of the cuticle was quantified again.
500 These data represent the post-chase counts.
501
502 **Generating *mlt-9(RNAi)* Cuticle Defects**
503 *mlt-9* RNAi was carried out as described previously (Frand et al., 2005; Kamath et al.,
504 2003) with some modifications as described in (Kamal et al., Manuscript Submitted).
505 Briefly, after plating 6,500 synchronized L1s on *mlt-9(RNAi)*-inducing HT115 *E. coil*
506 clones, the plates were stored at 16°C in the dark for 90 hours and then used in
507 dye/wactive experiments. Note that approximately 50% of *mlt-9(RNAi)*-treated worms
508 exhibit the expected cuticle defects. Performing mock RNAi with the empty L4440
509 plasmid failed to yield worms with obvious cuticle defects.
510
511 **Dye Staining**
512 Dye staining experiments were performed as previously described (Kamal et al.,
513 Manuscript Submitted). Briefly, Congo Red (CR) (Fisher chemical C580-25; CAS 573-58-0)

514 staining of worms was done with final concentration of 287 μM, made from a 14.4 mM
515 stock (i.e. a final concentration that is 0.02% made from a 1% stock (w/v) dissolved in
516 DMSO). Thioflavin S (ThS) (SIGMA, T1892) staining of worms was done with a final
517 concentration of 2.25 mM (made from a 225 mM stock) (i.e., a final concentration that
518 is a 0.1% solution from a 10% stock (w/v, dissolved in DMSO)). Note that ThS is a
519 complex mixture of molecules with two major species of 377.1 MW and 510.1 MW and
520 several other minor species (Enthammer et al., 2013). Given that the ratio of molecules
521 is unknown, we used an average MW of 443.6 for ThS in our calculations of molarity.
522 Eosin Y (EY) (Sigma-Aldrich, E4009) staining of worms was done with a final
523 concentration of 217 μM (from a working stock of 7.23 mM) (i.e. a final concentration of
524 0.15 mg/ml made from a 5 mg/mL stock (dissolved in 70% ethanol). Care must be taken
525 to remove excess EY dye from the worm sample by running worms on seeded plates for
526 at least 15 minutes prior to observation. Note that eosin Y stock should be stored at -
527 20°C and before its use, should be incubated at 55°C for ~2 minutes and vigorously
528 vortexed to ensure its solvation. Calcofluor White (CFW) (Fluorescent Brightener 28,
529 Sigma-Aldrich, CAS 4404-43-7) staining of worms was done with a final concentration of
530 52 μM (from a working stock of 10.4 mM) (i.e. a final concentration of 0.005% made
531 from a 1% stock (w/v, dissolved in DMSO 1% stock)). Unless otherwise noted, all staining
532 experiments were done in 500 μL of NGM for 3 hours in the dark, and then mounted
533 and imaged as described above.

534 **Dye Suppression Assays**

535 To test for the ability of dyes to suppress wact-190-induced worm lethality, 80 μL of
536 NGM containing HB101 bacteria (OD_{600} = 1.8-2.2) and 3.75 μM wact-190 was added to
537 each well of a 96-well plate, to which each dye was pinned (pinner model VP381N, V & P
538 Scientific, Inc) to a final concentration of 0, 0.94, 1.88, 3.75, 7.5, 15, 30, 60, 120, 240,
539 480 and 960 μM, in quadruplicates. 20 μL of M9 containing synchronized wildtype L1s
540 were then added to each well at ~50 L1/well. Three sets of controls were simultaneously
541 set up: wact-190 + DMSO (or 70% ethanol) (no dye), DMSO + dye (no wact-190) and
542 DMSO + DMSO (or 70% ethanol) (no wact-190, no dye). All samples were set up in
543 quadruplets (Day 0) and incubated at 20°C in a shaker @200 rpm. Worm viability was
544 scored on Day 6.

545 To test for the ability of dyes to suppress wact-190-induced crystal formation,
546 synchronized wildtype young adults were added (~ 1,000 worms in 50 μL) to a 1.5 mL
547 Eppendorf tube containing 500 μL NGM buffer and bacteria. Adult worms were either (i)
548 pre-incubated for 3 hours with 60 μM or 1200 μM of each dye or solvent (DMSO) only,
549 rinsed 3X with M9 buffer then incubated with 60 μM wact-190 in a fresh Eppendorf
550 tube, or (ii) co-incubated for 3 hours with 60 μM or 1200 μM of each dye (or solvent)
551 and 60 μM wact-190. Crystal formation was recorded by observing the birefringence of
552 the wact-190 crystals both in the presence and absence of the dye. wact-190 crystal
553 formation was compared with a negative control (no wact-190), that yielded no such
554 birefringence. All observations and imaging were carried out using 40X objective lens of

555 Leica DMRA2 compound microscope. The amount of birefringence was quantified using
556 Fiji/ImageJ software. 10-20 worms per sample were analyzed in 3 biological trials.
557
558 ***In vitro* Crystal Signal Emission Controls with and without Dye Staining**
559 To test for signal emission of wact-190 or wact-390 crystals themselves, as detected
560 with our fluorescent microscopy filter sets, 3 µL of a 10 mM wactive stock was first
561 added to 7 µL of water and mixed in a microcentrifuge tube, then directly added to a
562 microscope glass slide and coverslip applied. The appearance and birefringence of the
563 formed crystals were observed under DIC, birefringence, and fluorescence filter sets.
564 To test for whether the dyes specifically bind the *in vitro* precipitated crystals, the
565 same procedure was followed as above, but each dye was added at a final concentration
566 that was used in the dye staining experiments after the wactive precipitated in water.
567 Correlation between crystal birefringence (bright white dots in a dark background) and
568 dye fluorescence in their respective fluorescence channels was examined. All
569 observations were made using the 10X objective lens of the Leica DMRA2 compound
570 microscope.
571
572 **Statistics and Graphs**
573 Except where indicated, statistical differences were measured using a two-tailed
574 Students T-test. Dot plots were generated using Prism 8 graphing software.

575 **Animal Ethics Statement**

576 We (the authors) affirm that we have complied with all relevant ethical regulations for
577 animal testing and research. Given that our experiments focused exclusively on the
578 invertebrate nematode worm *C. elegans*, no ethical approval was required for any of the
579 presented work.

580

581 **Data Availability Statement**

582 Any primary data generated or analyzed during this study that are not included in this
583 published article and its supplementary information files are available upon request.

584 **Acknowledgements**

585 We thank Jack Daiyang Li for preliminary analyses. We thank David Hall, Zeynep Altun,
586 and Chris Crocker at WormAtlas for new artwork and permission to modify Worm Atlas
587 schematics. WormAtlas is funded by NIH OD 01943 to D.H. Hall. This work is supported
588 by CIHR grants (376634 and 313296) and a CRC to PJR.

589

590 **Author Contributions**

591 PJR and MK found that crystals form in the pharyngeal cuticle. MK performed the pulse-
592 chase and *mlt-9* experiments, the dye-staining experiments, the *in vitro* precipitation
593 experiments, and the detailed analysis of CR, ThS, EY, and CFW-suppression of death
594 and crystal formation. DH determined whether the fluorescent Spectrum suppressors
595 specifically stain the pharyngeal cuticle. DHH and KCQN performed the transmission
596 electron microscopy. JK performed additional small molecule screens that revealed new
597 crystal-forming compounds, performed the screen of the Spectrum library for
598 suppressors of crystal-induced death and follow-up work, and performed the network
599 analyses. ARB designed the novel 1,178-compound custom library, and identified the
600 crystallizer and suppressor analogs. PJR and MK composed figures and wrote the
601 manuscript with input from co-authors. PJR supervised and secured funding for the
602 project.

603

604 **Competing Interests**

605 The authors declare no competing interests.

606 **Literature Cited**

607 Ahmad, A., Ali, T., Park, H.Y., Badshah, H., Rehman, S.U., and Kim, M.O. (2017).
608 Neuroprotective Effect of Fisetin Against Amyloid-Beta-Induced Cognitive/Synaptic
609 Dysfunction, Neuroinflammation, and Neurodegeneration in Adult Mice. Mol Neurobiol
610 *54*, 2269-2285.

611 Akaishi, T., Morimoto, T., Shibao, M., Watanabe, S., Sakai-Kato, K., Utsunomiya-Tate, N.,
612 and Abe, K. (2008). Structural requirements for the flavonoid fisetin in inhibiting fibril
613 formation of amyloid beta protein. Neurosci Lett *444*, 280-285.

614 Altun, Z.F., and Hall, D.H. (2020). Handbook of C. elegans Anatomy. In WormAtlas.

615 Ayaz, M., Sadiq, A., Junaid, M., Ullah, F., Ovais, M., Ullah, I., Ahmed, J., and Shahid, M.
616 (2019). Flavonoids as Prospective Neuroprotectants and Their Therapeutic Propensity in
617 Aging Associated Neurological Disorders. Front Aging Neurosci *11*, 155.

618 Baker, L.G., Specht, C.A., Donlin, M.J., and Lodge, J.K. (2007). Chitosan, the deacetylated
619 form of chitin, is necessary for cell wall integrity in Cryptococcus neoformans. Eukaryot
620 Cell *6*, 855-867.

621 Banani, S.F., Lee, H.O., Hyman, A.A., and Rosen, M.K. (2017). Biomolecular condensates:
622 organizers of cellular biochemistry. Nat Rev Mol Cell Biol *18*, 285-298.

623 Banani, S.F., Rice, A.M., Peeples, W.B., Lin, Y., Jain, S., Parker, R., and Rosen, M.K. (2016).
624 Compositional Control of Phase-Separated Cellular Bodies. Cell *166*, 651-663.

625 Bennhold, H. (1922). Specific staining of amyloid by Congo red. Muenchen Med
626 Wochenschr *69*, 1537-1538.

627 Brady, J.P., Farber, P.J., Sekhar, A., Lin, Y.H., Huang, R., Bah, A., Nott, T.J., Chan, H.S.,
628 Baldwin, A.J., Forman-Kay, J.D.*, et al.* (2017). Structural and hydrodynamic properties of
629 an intrinsically disordered region of a germ cell-specific protein on phase separation.
630 Proc Natl Acad Sci U S A *114*, E8194-E8203.

631 Burns, A.R., Luciani, G.M., Musso, G., Bagg, R., Yeo, M., Zhang, Y., Rajendran, L., Glavin,
632 J., Hunter, R., Redman, E.*, et al.* (2015). Caenorhabditis elegans is a useful model for
633 anthelmintic discovery. Nat Commun *6*, 7485.

634 Caughey, W.S., Raymond, L.D., Horiuchi, M., and Caughey, B. (1998). Inhibition of
635 protease-resistant prion protein formation by porphyrins and phthalocyanines. Proc
636 Natl Acad Sci U S A *95*, 12117-12122.

637 Chen, C., Wang, Z., Zhang, Z., Liu, X., Kang, S.S., Zhang, Y., and Ye, K. (2018). The prodrug
638 of 7,8-dihydroxyflavone development and therapeutic efficacy for treating Alzheimer's
639 disease. Proc Natl Acad Sci U S A *115*, 578-583.

640 Chiti, F., and Dobson, C.M. (2017). Protein Misfolding, Amyloid Formation, and Human
641 Disease: A Summary of Progress Over the Last Decade. Annu Rev Biochem *86*, 27-68.

642 Choi, E.Y., Kang, S.S., Lee, S.K., and Han, B.H. (2020). Polyphenolic Biflavonoids Inhibit
643 Amyloid-Beta Fibrillation and Disaggregate Preformed Amyloid-Beta Fibrils. Biomol Ther
644 (Seoul) *28*, 145-151.

645 Cline, M.S., Smoot, M., Cerami, E., Kuchinsky, A., Landys, N., Workman, C., Christmas, R.,
646 Avila-Campilo, I., Creech, M., Gross, B.*, et al.* (2007). Integration of biological networks
647 and gene expression data using Cytoscape. Nat Protoc *2*, 2366-2382.

648 Cox, G.N., Kusch, M., and Edgar, R.S. (1981). Cuticle of Caenorhabditis elegans: its
649 isolation and partial characterization. J Cell Biol *90*, 7-17.

650 D'Souza, A., Szabo, A., Flynn, K.E., Dhakal, B., Chhabra, S., Pasquini, M.C., Weihrauch, D.,
651 and Hari, P.N. (2020). Adjuvant doxycycline to enhance anti-amyloid effects: Results
652 from the dual phase 2 trial. EClinicalMedicine *23*, 100361.

653 Divry, P.F., M. (1927). Sur les propriétées optiques de l'amyloide. C R Soc Biol *97*, 1808-
654 1810.

655 Dulovic, A., Renahan, T., Roseler, W., Rodelsperger, C., Rose, A.M., and Streit, A. (2020).
656 Rhabditophanes diutinus a parthenogenetic clade IV nematode with dauer larvae. PLoS
657 Pathog *16*, e1009113.

658 Enthammer, M., Papadakis, E.S., Salome Gachet, M., Deutsch, M., Schwaiger, S., Koziel,
659 K., Ashraf, M.I., Khalid, S., Wolber, G., Packham, G.*, et al.* (2013). Isolation of a novel
660 thioflavin S-derived compound that inhibits BAG-1-mediated protein interactions and
661 targets BRAF inhibitor-resistant cell lines. Mol Cancer Ther *12*, 2400-2414.

662 Farrawell, N.E., Yerbury, M.R., Plotkin, S.S., McAlary, L., and Yerbury, J.J. (2019). CuATSM
663 Protects Against the In Vitro Cytotoxicity of Wild-Type-Like Copper-Zinc Superoxide
664 Dismutase Mutants but not Mutants That Disrupt Metal Binding. ACS Chem Neurosci *10*,
665 1555-1564.

666 Frand, A.R., Russel, S., and Ruvkun, G. (2005). Functional genomic analysis of C. elegans
667 molting. PLoS Biol *3*, e312.

668 Fung, H.Y.J., Birol, M., and Rhoades, E. (2018). IDPs in macromolecular complexes: the
669 roles of multivalent interactions in diverse assemblies. Curr Opin Struct Biol *49*, 36-43.

670 Galford, K.F., and Jose, A.M. (2020). The FDA-approved drugs ticlopidine, sertaconazole,
671 and dexlansoprazole can cause morphological changes in C. elegans. Chemosphere *261*,
672 127756.

673 Geissen, M., Leidel, F., Eiden, M., Hirschberger, T., Fast, C., Bertsch, U., Tavan, P., Giese,
674 A., Kretzschmar, H., Schatzl, H.M.*, et al.* (2011). From high-throughput cell culture
675 screening to mouse model: identification of new inhibitor classes against prion disease.
676 ChemMedChem *6*, 1928-1937.

677 George-Raizen, J.B., Shockley, K.R., Trojanowski, N.F., Lamb, A.L., and Raizen, D.M.
678 (2014). Dynamically-expressed prion-like proteins form a cuticle in the pharynx of
679 Caenorhabditis elegans. Biol Open *3*, 1139-1149.

680 Gutierrez-Zepeda, A., Santell, R., Wu, Z., Brown, M., Wu, Y., Khan, I., Link, C.D., Zhao, B.,
681 and Luo, Y. (2005). Soy isoflavone glycitein protects against beta amyloid-induced
682 toxicity and oxidative stress in transgenic Caenorhabditis elegans. BMC Neurosci *6*, 54.

683 Harrington, B.J., and Raper, K.B. (1968). Use of a fluorescent brightener to demonstrate
684 cellulose in the cellular slime molds. Appl Microbiol *16*, 106-113.

685 Hirohata, M., Ono, K., Takasaki, J., Takahashi, R., Ikeda, T., Morinaga, A., and Yamada, M.
686 (2012). Anti-amyloidogenic effects of soybean isoflavones in vitro: Fluorescence
687 spectroscopy demonstrating direct binding to Abeta monomers, oligomers and fibrils.
688 Biochim Biophys Acta *1822*, 1316-1324.

689 Hole, K.L., and Williams, R.J. (2021). Flavonoids as an Intervention for Alzheimer's
690 Disease: Progress and Hurdles Towards Defining a Mechanism of Action. Brain Plast *6*,
691 167-192.

692 Iadanza, M.G., Jackson, M.P., Hewitt, E.W., Ranson, N.A., and Radford, S.E. (2018). A
693 new era for understanding amyloid structures and disease. Nat Rev Mol Cell Biol *19*,
694 755-773.

695 Jin, H.J., and Kaplan, D.L. (2003). Mechanism of silk processing in insects and spiders.
696 Nature *424*, 1057-1061.

697 Kamal, M., Moshiri, H., Magomedova, L., Han, D., Nguyen, K.C.Q., Yeo, M., Knox, J.,
698 Bagg, R., Won, A.M., Szlapa, K.*, et al.* (2019). The marginal cells of the Caenorhabditis
699 elegans pharynx scavenge cholesterol and other hydrophobic small molecules. Nat
700 Commun *10*, 3938.

701 Kamal, M., Tokmakjian, L., Knox, J., Mastrangelo, P., Ji, J., Cai, H., Wojciechowski, J.W.,
702 Hughes, M.P., Takács, K., Chu, X.*, et al.* (Manuscript Submitted). A Spatiotemporal
703 Reconstruction of the C. elegans Pharynx Cuticle Reveals a Tissue Rich in Phase-
704 Separating Proteins.

705 Kamath, R.S., Fraser, A.G., Dong, Y., Poulin, G., Durbin, R., Gotta, M., Kanapin, A., Le Bot,
706 N., Moreno, S., Sohrmann, M.*, et al.* (2003). Systematic functional analysis of the
707 Caenorhabditis elegans genome using RNAi. Nature *421*, 231-237.

708 Kim, J.K., Choi, S.J., Cho, H.Y., Hwang, H.J., Kim, Y.J., Lim, S.T., Kim, C.J., Kim, H.K.,
709 Peterson, S., and Shin, D.H. (2010). Protective effects of kaempferol (3,4',5,7-
710 tetrahydroxyflavone) against amyloid beta peptide (Abeta)-induced neurotoxicity in ICR
711 mice. Biosci Biotechnol Biochem *74*, 397-401.

712 Kimura, J., Shimizu, K., Kajima, K., Yokosuka, A., Mimaki, Y., Oku, N., and Ohizumi, Y.
713 (2018). Nobiletin Reduces Intracellular and Extracellular beta-Amyloid in iPS Cell-Derived
714 Alzheimer's Disease Model Neurons. Biol Pharm Bull *41*, 451-457.

715 Knight, C.G., Patel, M.N., Azevedo, R.B., and Leroi, A.M. (2002). A novel mode of
716 ecdysozoan growth in Caenorhabditis elegans. Evol Dev *4*, 16-27.

717 Kumar, S.K., Dispenzieri, A., and Lacy, M.Q. (2012). Doxycycline used as Post Transplant
718 antibacterial prophylaxis improves survival in patients with light chain amyloidosis
719 undergoing autologous stem cell transplantation. Blood *120*, 3138.

720 Kwok, T.C., Ricker, N., Fraser, R., Chan, A.W., Burns, A., Stanley, E.F., McCourt, P., Cutler,
721 S.R., and Roy, P.J. (2006). A small-molecule screen in C. elegans yields a new calcium
722 channel antagonist. Nature *441*, 91-95.

723 Larbig, G., Pickhardt, M., Lloyd, D.G., Schmidt, B., and Mandelkow, E. (2007). Screening
724 for Inhibitors of Tau Protein Aggregation into Alzheimer Paired

725 Helical Filaments: A Ligand Based Approach Results in Successful Scaffold

726 Hopping. Current Alzheimer Research *4*, 315-323.

727 Lee, B.I., Lee, S., Suh, Y.S., Lee, J.S., Kim, A.K., Kwon, O.Y., Yu, K., and Park, C.B. (2015).
728 Photoexcited Porphyrins as a Strong Suppressor of beta-Amyloid Aggregation and
729 Synaptic Toxicity. Angew Chem Int Ed Engl *54*, 11472-11476.

730 Makin, S. (2018). The amyloid hypothesis on trial. Nature *559*, S4-S7.

731 McAlary, L., Plotkin, S.S., Yerbury, J.J., and Cashman, N.R. (2019). Prion-Like Propagation
732 of Protein Misfolding and Aggregation in Amyotrophic Lateral Sclerosis. Front Mol
733 Neurosci *12*, 262.

734 Muiznieks, L.D., Sharpe, S., Pomes, R., and Keeley, F.W. (2018). Role of Liquid-Liquid
735 Phase Separation in Assembly of Elastin and Other Extracellular Matrix Proteins. J Mol
736 Biol *430*, 4741-4753.

737 Mullard, A. (2021). Landmark Alzheimer's drug approval confounds research
738 community. Nature *594*, 309-310.

739 O'Boyle, N.M., Banck, M., James, C.A., Morley, C., Vandermeersch, T., and Hutchison,
740 G.R. (2011). Open Babel: An open chemical toolbox. J Cheminform *3*, 33.

741 Obici, L., Cortese, A., Lozza, A., Lucchetti, J., Gobbi, M., Palladini, G., Perlini, S., Saraiva,
742 M.J., and Merlini, G. (2012). Doxycycline plus tauroursodeoxycholic acid for
743 transthyretin amyloidosis: a phase II study. Amyloid *19 Suppl 1*, 34-36.

744 Panche, A.N., Diwan, A.D., and Chandra, S.R. (2016). Flavonoids: an overview. J Nutr Sci
745 *5*, e47.

746 Risi, G., Aguilera, E., Lados, E., Suarez, G., Carrera, I., Alvarez, G., and Salinas, G. (2019).
747 Caenorhabditis elegans Infrared-Based Motility Assay Identified New Hits for Nematicide
748 Drug Development. Vet Sci *6*.

749 Rowe, D., Mathers, S., Smith, G., Windebank, E., Rogers, M.-L., Noel, K., and Rosenfeld,
750 C.S. (2018). Theme 9 Clinical trials and trial design: CLT-26 Modification of ALS disease
751 progression in a phase 1 trial of CuATSM. Paper presented at: Amyotrophic Lateral
752 Sclerosis and Frontotemporal Degeneration Symposium.

753 Schmidt, H.B., and Gorlich, D. (2016). Transport Selectivity of Nuclear Pores, Phase
754 Separation, and Membraneless Organelles. Trends Biochem Sci *41*, 46-61.

755 Schüller, A., Hähnke, V., and Schneider, G. (2007). SmiLib v2.0: A Java-Based Tool for
756 Rapid Combinatorial Library Enumeration. QSAR & Combinatorial Science *3*, 407-410.

757 Sevigny, J., Chiao, P., Bussiere, T., Weinreb, P.H., Williams, L., Maier, M., Dunstan, R.,
758 Salloway, S., Chen, T., Ling, Y*., et al.* (2016). The antibody aducanumab reduces Abeta
759 plaques in Alzheimer's disease. Nature *537*, 50-56.

760 Slotta, U., Hess, S., Spiess, K., Stromer, T., Serpell, L., and Scheibel, T. (2007). Spider silk
761 and amyloid fibrils: a structural comparison. Macromol Biosci *7*, 183-188.

762 Somerville, A.N. (1998). SciFinder Scholar. Journal of Chemical Education *75*, 959-960.

763 Sterling, T., and Irwin, J.J. (2015). ZINC 15--Ligand Discovery for Everyone. J Chem Inf
764 Model *55*, 2324-2337.

765 Tan, Y., Hoon, S., Guerette, P.A., Wei, W., Ghadban, A., Hao, C., Miserez, A., and Waite,
766 J.H. (2015). Infiltration of chitin by protein coacervates defines the squid beak
767 mechanical gradient. Nat Chem Biol *11*, 488-495.

768 Vassar, P.S., and Culling, C.F. (1959). Fluorescent stains, with special reference to
769 amyloid and connective tissues. Arch Pathol *68*, 487-498.

770 Vernon, R.M., and Forman-Kay, J.D. (2019). First-generation predictors of biological
771 protein phase separation. Curr Opin Struct Biol *58*, 88-96.

772 Wang, L., Zeng, R., Pang, X., Gu, Q., and Tan, W. (2015). The mechanisms of flavonoids
773 inhibiting conformational transition of amyloid-b42 monomer: a comparative molecular
774 dynamics simulation study. RSC Advances *5*, 66391-66402.

775 Watanabe, H., Ono, M., Ikeoka, R., Haratake, M., Saji, H., and Nakayama, M. (2009).
776 Synthesis and biological evaluation of radioiodinated 2,5-diphenyl-1,3,4-oxadiazoles for
777 detecting beta-amyloid plaques in the brain. Bioorg Med Chem *17*, 6402-6406.

778 Wei, D., Tang, J., Bai, W., Wang, Y., and Zhang, Z. (2014a). Ameliorative effects of
779 baicalein on an amyloid-beta induced Alzheimer's disease rat model: a proteomics
780 study. Curr Alzheimer Res *11*, 869-881.

781 Wei, W., Tan, Y., Martinez Rodriguez, N.R., Yu, J., Israelachvili, J.N., and Waite, J.H.
782 (2014b). A mussel-derived one component adhesive coacervate. Acta Biomater *10*,
783 1663-1670.

784 Wright, K.A., and Thomson, J.N. (1981). The buccal capsule of Caenorhabditis elegans
785 (Nematodea:Rhabditoidea): an ultrastructural study. Canadian Journal of Zoology *59*,
786 1952-1961.

787 Yang, Y., Cui, M., Zhang, X., Dai, J., Zhang, Z., Lin, C., Guo, Y., and Liu, B. (2014).
788 Radioiodinated benzyloxybenzene derivatives: a class of flexible ligands target to beta-
789 amyloid plaques in Alzheimer's brains. J Med Chem *57*, 6030-6042.

790 Yin, F., Liu, J., Ji, X., Wang, Y., Zidichouski, J., and Zhang, J. (2011). Silibinin: a novel
791 inhibitor of Abeta aggregation. Neurochem Int *58*, 399-403.

792 Yuan, C., and Gao, Z. (2013). Abeta interacts with both the iron center and the porphyrin
793 ring of heme: mechanism of heme's action on Abeta aggregation and disaggregation.
794 Chem Res Toxicol *26*, 262-269.

795 Zhang, Y., Foster, J.M., Nelson, L.S., Ma, D., and Carlow, C.K. (2005). The chitin synthase
796 genes chs-1 and chs-2 are essential for C. elegans development and responsible for
797 chitin deposition in the eggshell and pharynx, respectively. Dev Biol *285*, 330-339.

798

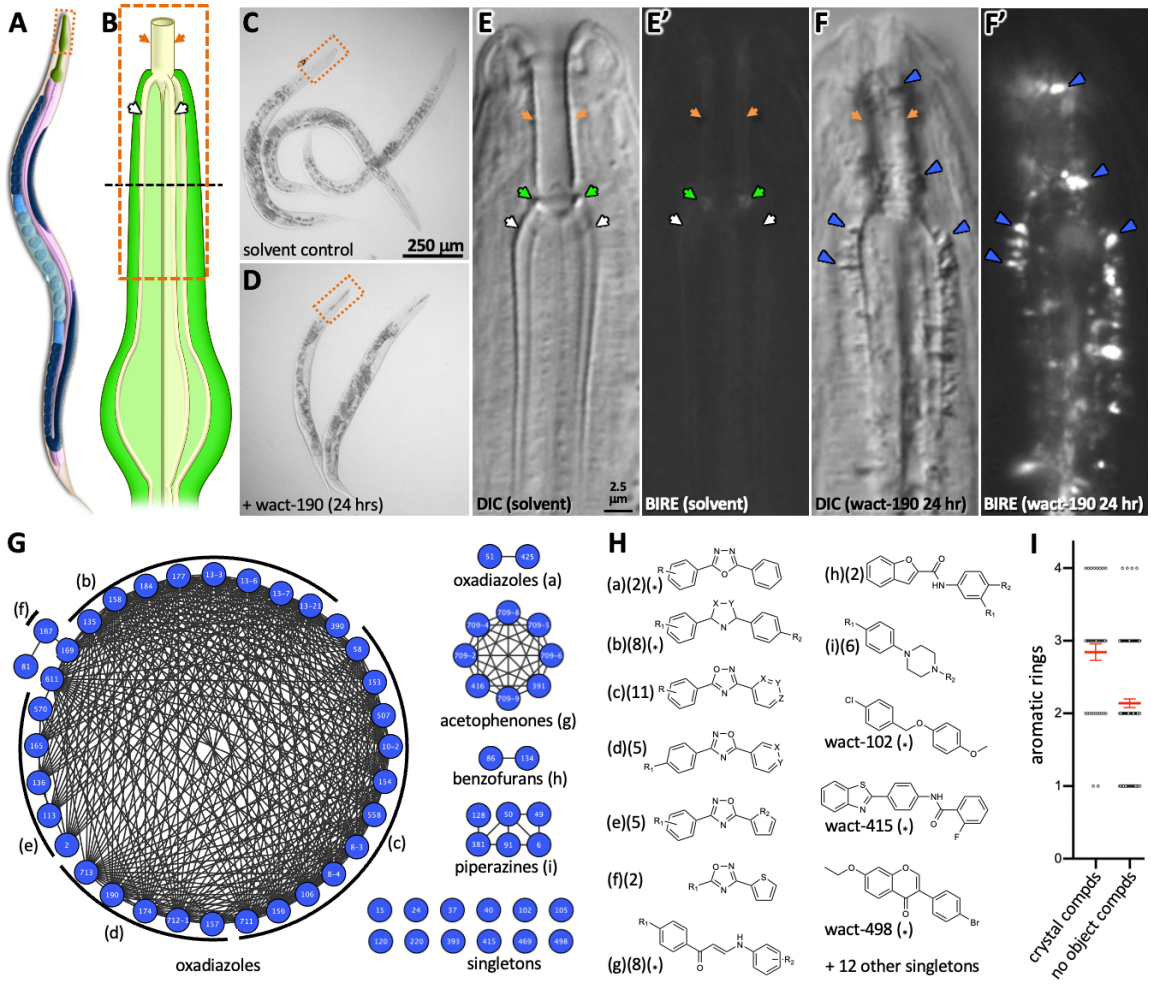

Figure 1. 24 Small Molecule Scaffolds are Capable of Crystal Formation. A. A schematic of *C. elegans* anatomy (from WormAtlas; used with permission). The pharynx is green. **B.** A schematic of the corpus that is the subject of panels C-F. The central lumen is indicated in dark grey, the channels and buccal cavity are in cream. The black dashed line corresponds to the approximate cross sections shown in Figure 2. **C-D.** Photos of worms taken at the working dissection microscope illustrating the obviousness of wact-190 crystal formation relative to the control. The orange boxed area corresponds to the area highlighted in A and B. The scale bar in C also applies to D. **E.** Anterior-most region of a worm treated with solvent only. Orange arrows indicate the

809 buccal cavity cuticle, the green arrows highlight the buccal collar, and the white arrows
810 indicate the cuticle that lines the channels. Differential interference contrast (DIC) and
811 birefringent (BIRE) images are shown. The scale bar in E applies to all images in the
812 upper right-hand side. **F.** Anterior-most region of a worm treated with 30 μM wact-190
813 for 24 hours. The notation is the same as that in E. Blue arrowheads highlight the
814 birefringent crystals. **G.** An unsupervised structural similarity network of the crystalizing
815 molecules. Each node represents a small molecule, labelled with a wactive number. The
816 link represents a Tanimoto structural similarity coefficient of the core scaffold of 0.6 or
817 higher on the Tanimoto scale. The lower-case labels indicate groups of molecules with
818 the same core scaffolds as indicated in H. Note that the unsupervised network links the
819 non-piperazine wact-128 to the piperazine cluster and leaves the piperazine wact-220 as
820 a singleton because of structural differences beyond the piperazine group in the
821 scaffold. **H.** Markush representations of the core scaffolds of structural analogs able to
822 crystalize in the worm. R, X, Y, and Z groups are shown in Supplemental Figure 1. The 15
823 singletons shown correspond to the 12 singleton nodes shown in G, plus three
824 additional molecules (wact-81, wact-390, and wact-611) within the largest cluster of G.
825 Asterisks indicate literature-based evidence for analogs with the same core scaffold able
826 to bind amyloid fibrils *in vitro* as described in the main text and in Supplemental Figure
827 1. **I.** Crystalizing molecules from the wactive library (Burns et al., 2015) have significantly
828 more aromatic rings (calculated using Open Babel (O'Boyle et al., 2011)) compared to
829 non-crystalizing molecules from the same library (p=9E-8). The mean and standard error
830 is shown.
831

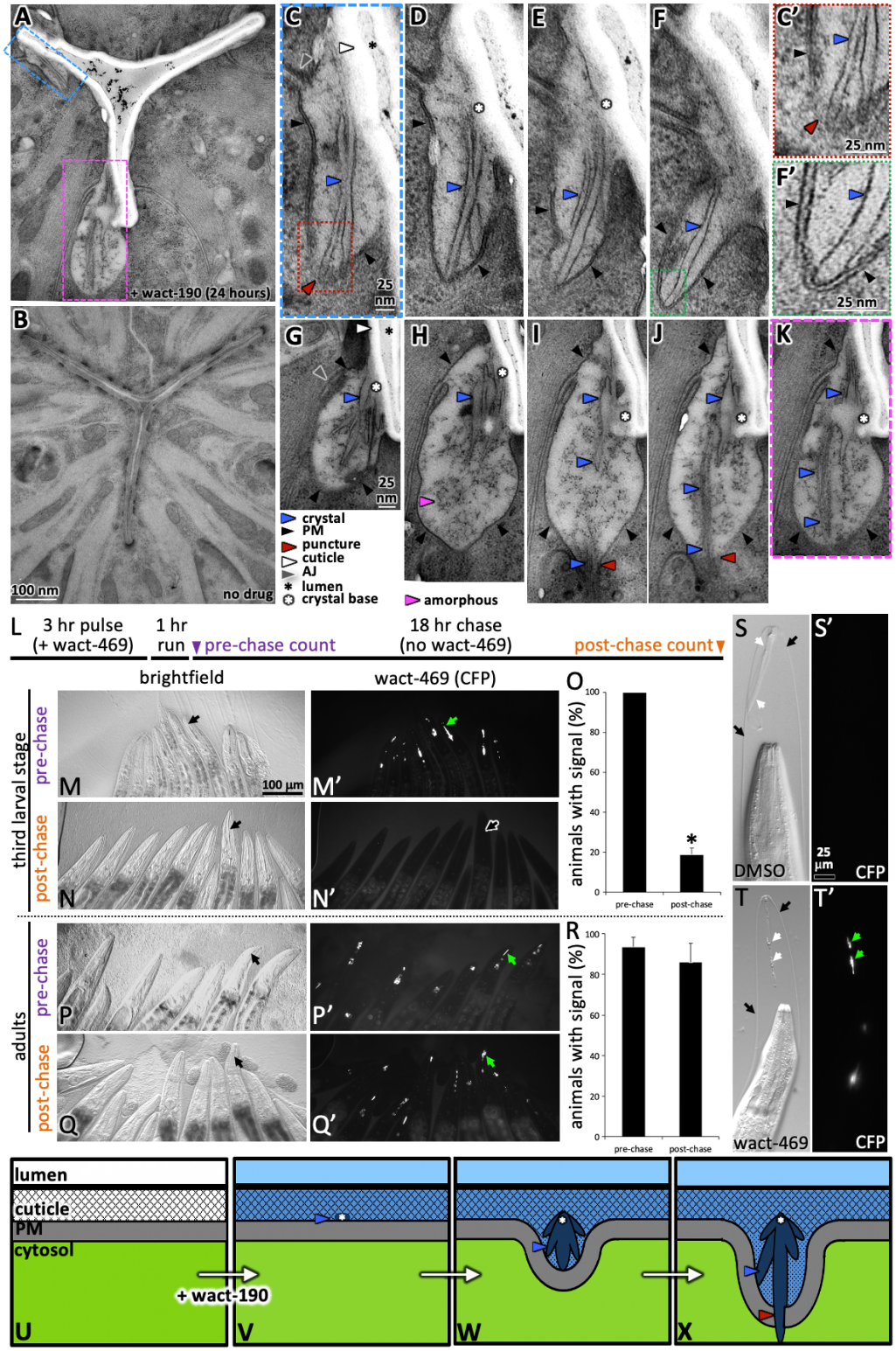

Figure 2. Wact-190 Crystals Form in Association with the Pharyngeal Cuticle. A-B.

Transmission electron microscopy of cross sections of wild type worms incubated with

836 either 30 μM wact-190 (A) or solvent control (DMSO; B). The scale bar in B also applies
837 to A. **C-F.** Serial sections of the area indicated in the blue box in 'A' ('C' is the actual
838 section of the series highlighted in 'A'). The scale in C applies to C-F. **C'.** An enlargement
839 of the area boxed in 'C' showing how the object (blue arrowhead) is disrupting the
840 plasma membrane. **F'.** An enlargement of the area boxed in 'F' showing how the object
841 (blue arrowhead) is juxtaposed to the plasma membrane (black arrowheads). **G-K.** Serial
842 sections of the area indicated in the pink box in 'A' ('K' is the section of the series
843 highlighted in 'A'). The scale in G applies to G-K. **L.** A timeline of the pulse-chase
844 experiment. **M-N.** Examples of third larval stage animals that have been incubated in
845 fluorescent wact-469 (60 μM) before the chase (M) or after the chase (N). The scale in
846 M applies to M-Q'. **O.** Quantification of the fraction of animals with fluorescent wact-
847 469 crystals. The asterisk indicates a significant difference (p<0.001) relative to pre-
848 chase using a Student's t-test. Standard error of the mean is shown. **P-R.** Analogous to
849 M-O, but done with young adult animals. **S&T.** *mlt-9(RNAi)* animals with incompletely
850 separated pharyngeal cuticle (black arrows) exposed to either DMSO (S) or wact-469 (60
851 μM) (T) for 3 hours. wact-469 crystals are indicated with green arrows. The scale in S
852 applies to S-T'. **U-X.** The interpretation of how and where crystals form in relation to the
853 pharyngeal cuticle and the plasma membrane of the underlying marginal cells. The
854 relative concentration of wact-190 is depicted in shades of blue; the darker the shade,
855 the greater the relative concentration. The legend for the arrows and asterisks in U-X
856 are indicated below panels G and K.

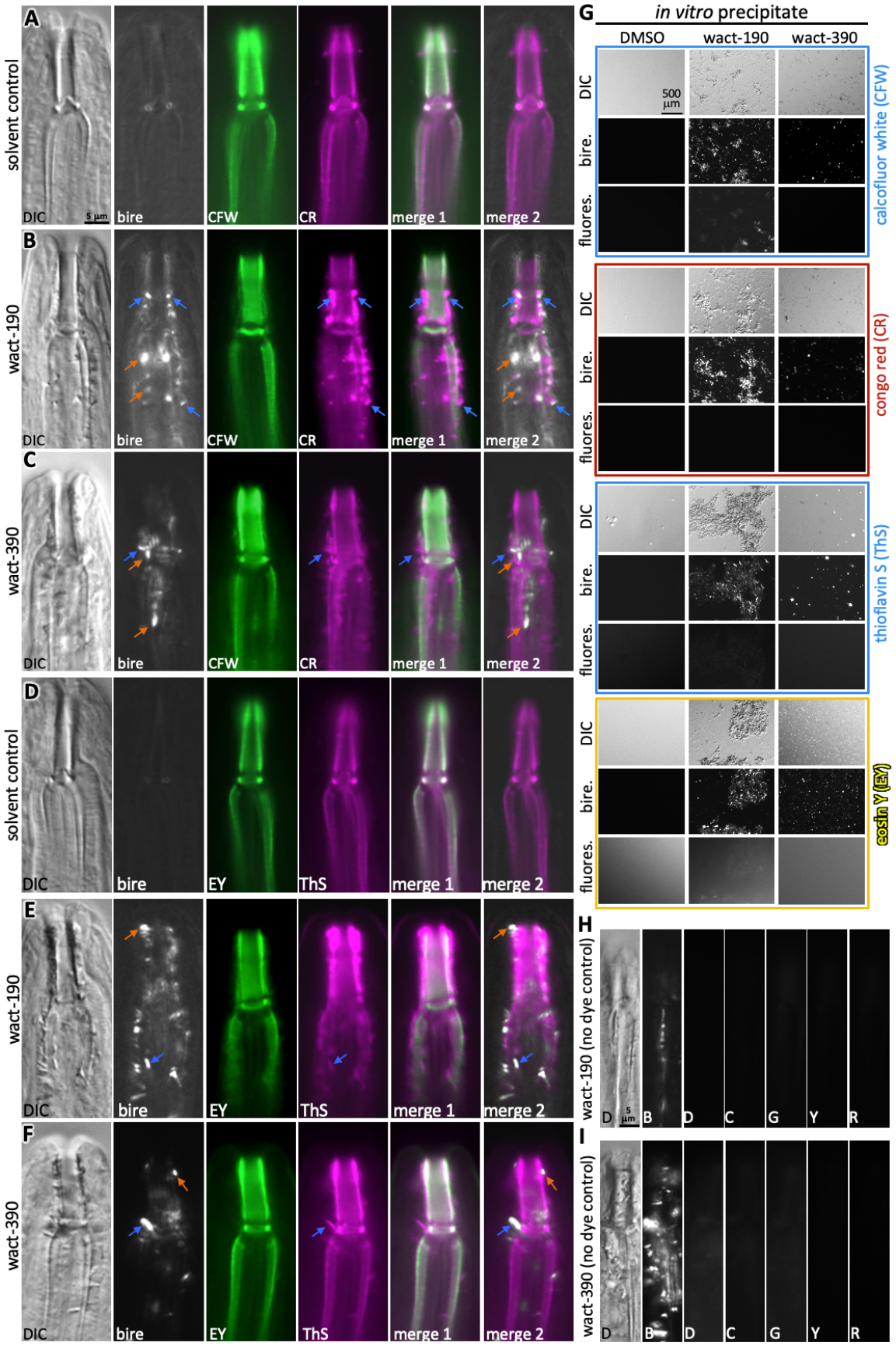
A
solvent control
DIC
5 µm
bire
CFW
CR
merge 1
merge 2
B
wact-190
C
wact-390
D
EY
ThS
E
F
G
in vitro precipitate
DMSO
wact-190
wact-390
DIC
bire.
fluores.
500 µm
calcofluor white (CFW)
congo red (CR)
thioflavin S (ThS)
eosin Y (EY)
H
wact-190 (no dye control)
D
B
C
G
Y
R
I
wact-390 (no dye control)

857

858 **Figure 3. Crystals Preferentially Disrupt Amyloid Dye-Staining Material of the**
859 **Pharyngeal Cuticle. A-F.** Images of the anterior-most end of the worm**.** The imaging
860 channel is indicated (lower left) as is the wactive treatment (left-hand side of
861 micrograph series). DIC, differential interference contrast; bire, birefringence; CFW,
862 calcofluor white; ThS, thioflavin S; EY, eosin Y. Merge 1 is the merge of the two dye
863 signals. Merge 2 is the merge of the signals from the amyloid-binding dye and
864 birefringence. Blue arrows indicate overlapping signals of the amyloid-binding dye and
865 birefringence; orange arrows show a lack of amyloid-binding dye signal associated with
866 birefringence signal. The scale in A applies to A-F. **G.** Control for the ability of dyes to
867 bind wactive crystals. Precipitate of wact-190 or wact-390 was formed in solution (or
868 DMSO solvent control) and was subsequently stained with the dye indicated on the right
869 of each set. The dyes were used at the same concentration as the *in vivo* staining
870 experiments as described in the methods. Each condition was imaged using DIC,
871 birefringence (bire) or the appropriate fluorescent (floures.) channel, as indicated on the
872 left of each panel, but not rinsed from the slide, which accounts for the non-specific
873 signal in the EY fluorescent channel. The scale in the upper left micrograph applies to all
874 images in G. **H-I.** Controls for the fluorescence of crystals in the different channels. D,
875 differential interference contrast (DIC); B, birefringence; C, CFP; G, GFP; Y, YFP; R, RFP
876 channels. The scale bar in H also applies to I. 60 μM of wact-190 and wact-390 was used
877 in all experiments relevant to panels A-I.

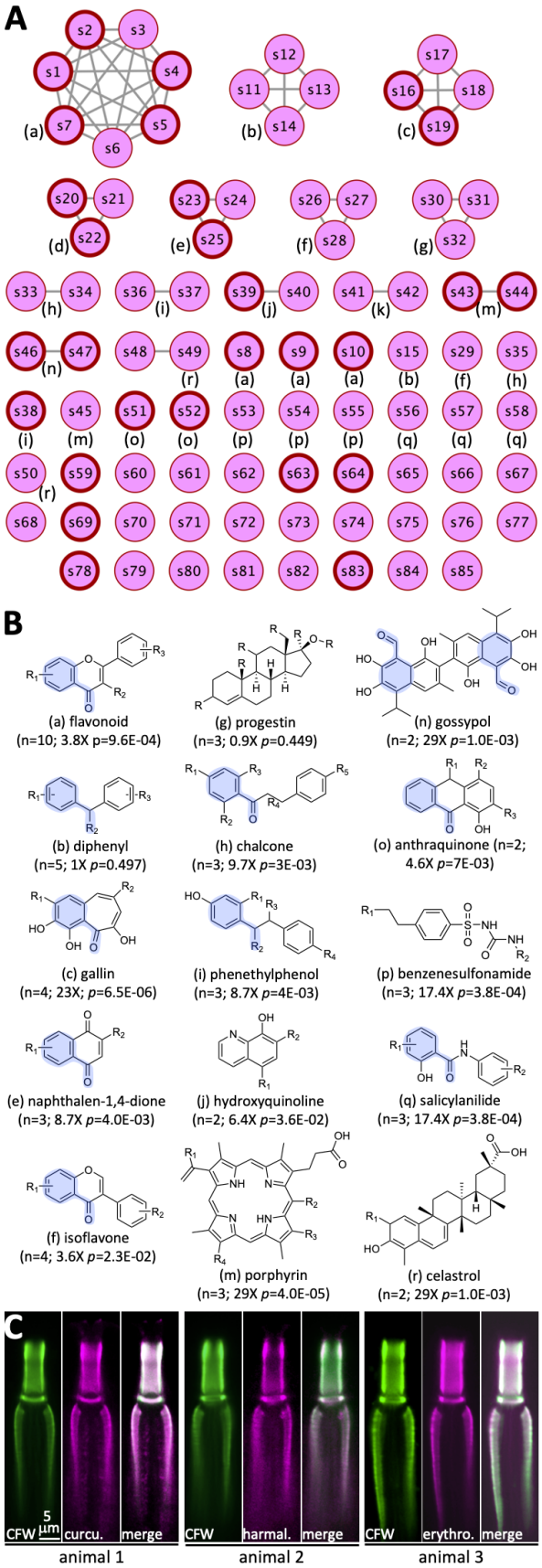
A
(a) s1 s2 s3 s4 s5 s6 s7
(b) s11 s12 s13 s14
(c) s16 s17 s18 s19
(d) s20 s21 s22
(e) s23 s24 s25
(f) s26 s27 s28
(g) s30 s31 s32
(h) s33 s34
(i) s36 s37
(j) s39 s40
(k) s41 s42
(m) s43 s44
(n) s46 s47
(r) s48 s49
(a) s8
(a) s9
(a) s10
(b) s15
(f) s29
(h) s35
(i) s38
(m) s45
(o) s51
(o) s52
(p) s53
(p) s54
(p) s55
(q) s56
(q) s57
(q) s58
(r) s50
s59 s60 s61 s62 s63 s64 s65 s66 s67
s68 s69 s70 s71 s72 s73 s74 s75 s76 s77
s78 s79 s80 s81 s82 s83 s84 s85
B
(a) flavonoid
(n=10; 3.8X p=9.6E-04)
(g) progestin
(n=3; 0.9X p=0.449)
(n) gossypol
(n=2; 29X p=1.0E-03)
(b) diphenyl
(n=5; 1X p=0.497)
(h) chalcone
(n=3; 9.7X p=3E-03)
(o) anthraquinone (n=2;
4.6X p=7E-03)
(c) gallin
(n=4; 23X; p=6.5E-06)
(i) phenethylphenol
(n=3; 8.7X p=4E-03)
(p) benzenesulfonamide
(n=3; 17.4X p=3.8E-04)
(e) naphthalen-1,4-dione
(n=3; 8.7X p=4.0E-03)
(j) hydroxyquinoline
(n=2; 6.4X p=3.6E-02)
(q) salicylanilide
(n=3; 17.4X p=3.8E-04)
(f) isoflavone
(n=4; 3.6X p=2.3E-02)
(m) porphyrin
(n=3; 29X p=4.0E-05)
(r) celastrol
(n=2; 29X p=1.0E-03)
C
5 µm
CFW curcu. merge
CFW harmal. merge
CFW erythro. merge
animal 1
animal 2
animal 3

878

879 **Figure 4. A Screen for wact-190 Suppressors Reveals Amyloid-Disrupting Molecules. A.**
880 A structural similarity network of the 85 Spectrum library hits that suppress wact-190
881 lethality and crystal formation. The nodes (circles) represent a drug or natural product.
882 The links (straight lines) represent a Tanimoto structural similarity coefficient of 0.8 or
883 more (see methods). A bold red outline indicates known disruptors of amyloid fibril
884 formation. See Supplementary Table 1 for details and names of the compounds. **B.** Core
885 scaffolds among the drug suppressors of crystal formation. The small case letter
886 preceding the scaffold name corresponds to the nodes indicated in (A). The number (n)
887 of individual molecules within the network is indicated, as is the enrichment of that
888 scaffold within the network relative to that expected by random chance based on the
889 prevalence of that scaffold within the entire library (the hypergeometric *p* value is
890 shown). The benzaldehyde substructure is highlighted in blue. **C.** Examples of the
891 localization of crystal suppressors (60 μM) that are fluorescent. Calcofluor white (CFW)
892 is used as a counter-stain control; curcu., curcumin; harmal., harmaline; erythro.,
893 erythrosine. See Supplemental Figure 4 for additional examples and controls. The scale
894 in 'C' applies to all images in the series.

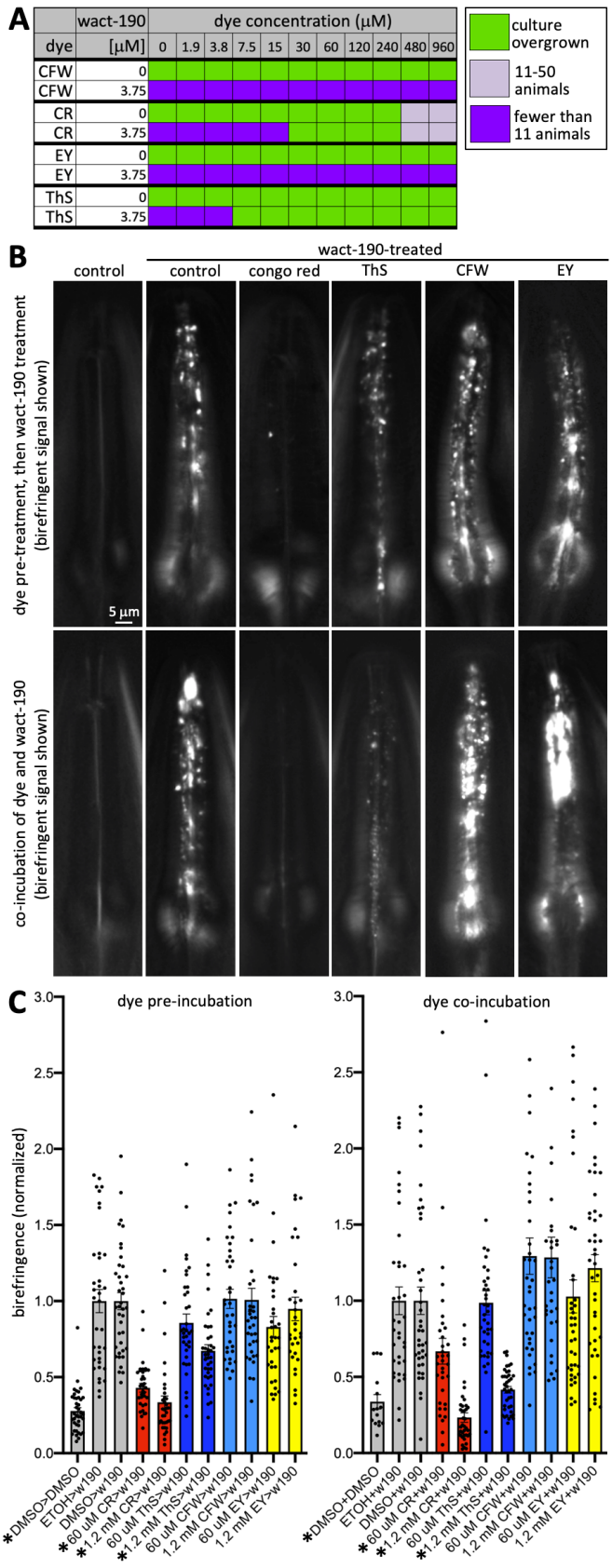
A
wact-190
dye concentration (μM)
dye
[μM]
0
1.9
3.8
7.5
15
30
60
120
240
480
960
CFW 0
CFW 3.75
CR 0
CR 3.75
EY 0
EY 3.75
ThS 0
ThS 3.75
culture overgrown
11-50 animals
fewer than 11 animals
B
wact-190-treated
control
control
congo red
ThS
CFW
EY
dye pre-treatment, then wact-190 treatment (birefringent signal shown)
co-incubation of dye and wact-190 (birefringent signal shown)
5 μm
C
dye pre-incubation
dye co-incubation
birefringence (normalized)
*DMSO>DMSO
ETOH>w190
DMSO>w190
*60 uM CR>w190
*1.2 mM CR>w190
60 uM ThS>w190
*1.2 mM ThS>w190
60 uM CFW>w190
1.2 mM CFW>w190
60 uM EY>w190
1.2 mM EY>w190
*DMSO+DMSO
ETOH+w190
DMSO+w190
*60 uM CR+w190
*1.2 mM CR+w190
60 uM ThS+w190
*1.2 mM ThS+w190
60 uM CFW+w190
1.2 mM CFW+w190
60 uM EY+w190
1.2 mM EY+w190

895

896 **Figure 5. Amyloid-Binding Dyes Suppress Crystal Formation. A.** Six-day viability assay
897 results illustrating that amyloid binding dyes (CR and ThS) can suppress wact-190-
898 induced lethality, but that chitin/chitosan-binding dyes (CFW and EY) cannot. Each cell
899 shows the summary of 3 trials each done in quadruplicate. **B-C.** Amyloid-binding dyes,
900 but not chitin/chitosan-binding dyes, can suppress crystal formation. On the top row,
901 animals have been pre-incubated in the indicated dye or solvent control for 3 hours.
902 Then, the right-most five samples were incubated in 60 μM wact-190 for three hours
903 without the initial dyes present. On the bottom row of (B), animals have been incubated
904 in the indicated dye or solvent control, and for the five right-most five samples,
905 simultaneously incubated with wact-190 (60 μM) for 3 hours. Representative
906 birefringence images are shown in (B) and the corresponding signal quantification is
907 reported in (C). The scale bar in the upper left of B applies to all images in the series.
908 Samples labelled with an asterisk indicates a significant difference relative to control
909 (p<0.01). Standard error of the mean is shown.

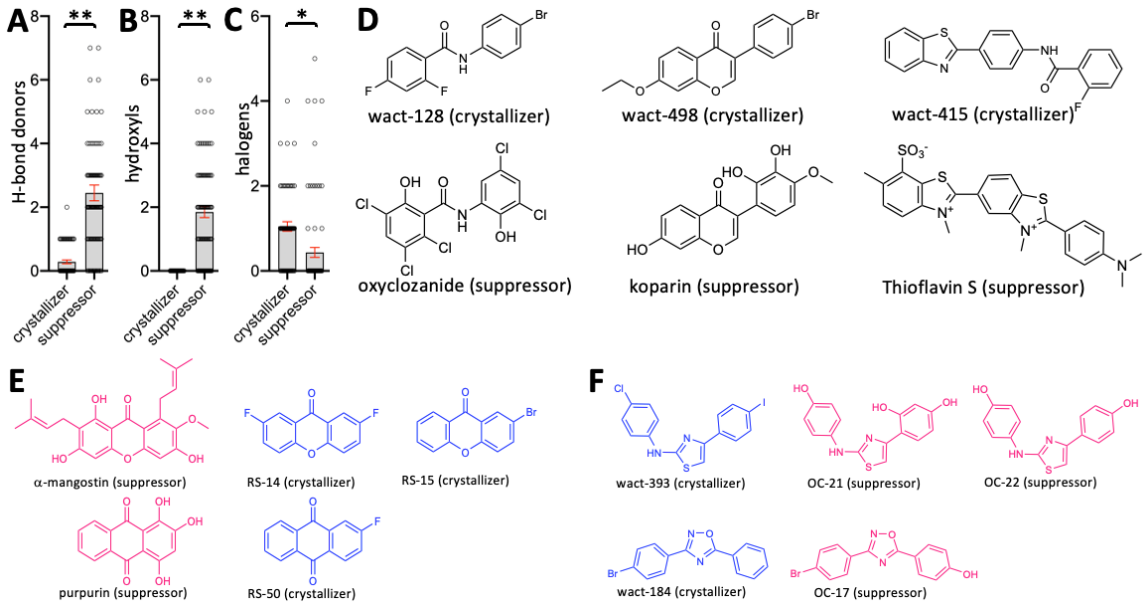

Figure 6. Crystallizers and Suppressors can Share Identical Core Structures. A-C. Graphs of the indicated physicochemical features of crystallizers and suppressors. A single and double asterisk indicate $p<0.001$ and $p<1.0E-10$, respectively. Standard error of the mean is shown. **D.** Crystallizers and suppressors that share an identical or similar core structure. **E.** Core scaffolds of suppressing molecules that can be turned into crystallizers (see Supplemental Table 2 for additional details). **F.** Core scaffolds of crystallizing molecules that can be turned into suppressors (see Supplemental Table 3 for additional details).

Node ID[a]	cluster[b]	Name of Molecule	viability assay[c] DMSO n=2	w190 3.8 uM n=5	w11 10 uM n=3	Crystal Formation Assay[d] wact-190 + suppressor % crystals	n	SD	p value	Evidence for anti-amyloid activity (PubMed ID or Patent Number)[e]	Targeted Amyloid in Study
		solvent control	OG	0	0	100	4	0	na	none found	na
s1	a	RHAMNETIN	OG	OG	0	0	2	0	0.0E+00	16248550	Abeta42
s2	a	BAICALEIN	OG	OG	0	42	3	25	1.6E-02	25043951, 23686791, 25043951, 25274114	Abeta42, IAPP
s3	a	NOBILETIN	OG	OG	0	7	2	10	5.4E-03	none found	na
s4	a	MORIN	OG	OG	0	27	4	40	1.0E-02	22762350, 16248550	Abeta42
s5	a	FISETIN	OG	OG	0	29	2	11	1.2E-02	16248550, 18761054, 26944285	Abeta42
s6	a	6,7-DIHYDROXYFLAVONE	OG	OG	0	0	2	0	0.0E+00	none found	na
s7	a	KAEMPFEROL	OG	OG	0	4	2	5	1.5E-03	24468532, 16248550	Amylodosis, Abeta42, IAPP
s8	a	HESPERETIN	OG	OG	0	20	4	15	4.0E-05	28672874, 22383310	Abeta42
s9	a	SILIBININ	OG	OG	0	18	2	3	6.9E-04	21185897, 19552690	Abeta42
s10	a	ISOGINKGETIN	OG	OG	0	3	2	4	8.6E-04	31697876	Abeta42
s11	b	DICHLOROPHEN	sick	sick	0	19	4	26	7.6E-04	none found	na
s12	b	2,3,4-TRIHYDROXY-4'-ETHOXYBENZOPHENONE	OG	OG	0	14	3	12	2.3E-04	none found	na
s13	b	3,4-DIDESMETHYL-5-DESHYDROXY-3'-ETHOXYSCLEROIN	OG	OG	0	20	4	13	1.7E-05	none found	na
s14	b	CLOFOCTOL	OG	OG	0	0	2	0	0.0E+00	none found	na
s15	b	ROSOLIC ACID	OG	OG	0	70	2	1	1.6E-04	none found	na
s16	c	PYROGALLIN	OG	OG	0	15	4	20	1.4E-04	US9463195B2	β-2 microglobulin fibril
s17	c	PURPUROGALLIN-4-CARBOXYLIC ACID	OG	OG	0	74	2	0	1.6E-04	none found	na
s18	c	METHYL 7-DESHYDROXYPYROGALLIN-4-CARBOXYLATE	OG	OG	0	0	2	0	0.0E+00	US9463195B2	β-2 microglobulin fibril
s19	c	PURPUROGALLIN	OG	OG	0	0	2	0	0.0E+00	15611092, US9463195B2	Tau, β-2 microglobulin fibril
s20	d	2,4-DINITROPHENOL	OG	OG	0	9	3	16	5.3E-04	16627944, 11344119, 11913969	TTR amyloid
s21	d	OCTINOXATE	OG	OG	0	12	2	17	1.8E-02	none found	na
s22	d	DIIODOTYROSINE DIHYDRATE	OG	OG	0	11	2	7	2.7E-03	US20050038117A1	multiple
s23	e	LAWSONE	OG	OG	0	22	2	7	4.4E-03	30704121	TTR amyloid
s24	e	ANTHRACENE-1,4-DIONE	OG	OG	0	21	2	13	1.3E-02	none found	na
s25	e	1,4-NAPHTHOQUINONE	OG	OG	0	0	2	0	0.0E+00	20709023, 31016960	Abeta42
s26	f	ISOPOMIFERIN	OG	OG	0	2	3	3	6.1E-07	none found	na
s27	f	ISOOSAJIN	OG	OG	0	21	2	13	1.2E-02	none found	na
s28	f	MUNDULONE ACETATE	OG	OG	0	13	2	13	1.1E-02	none found	na
s29	f	KOPARIN	OG	OG	0	12	2	11	7.5E-03	none found	na
s30	g	PREGNENOLONE SUCCINATE	OG	OG	0	0	3	0	0.0E+00	none found	na
s31	g	DESOGESTREL	OG	OG	0	17	2	8	4.4E-03	none found	na
s32	g	NORGESTIMATE	OG	OG	0	10	2	1	2.5E-05	none found	na
s33	h	2',4'-DIHYDROXYCHALCONE	OG	OG	0	0	3	0	0.0E+00	none found	na
s34	h	4'-HYDROXYCHALCONE	OG	OG	0	0	2	0	0.0E+00	none found	na
s35	h	PHLORETIN	OG	OG	0	5	2	2	1.8E-04	none found	na
s36	i	DIENESTROL	OG	OG	0	0	2	0	0.0E+00	none found	na
s37	i	ONONETIN	OG	OG	0	0	3	0	0.0E+00	none found	na
s38	i	DIETHYLSTILBESTROL	OG	OG	0	0	3	0	0.0E+00	15469931	amyloidosis
s39	j	CLIOQUINOL	OG	OG	0	9	2	13	9.9E-03	14676042, 21199452, 24591589	Abeta42
s40	j	NITROXOLINE	OG	OG	0	53	4	35	3.7E-02	none found	na
s41	k	MYCOPHENOLIC ACID	OG	OG	0	12	2	10	6.8E-03	none found	na
s42	k	BENZYL BENZOATE	OG	OG	0	8	2	1	4.3E-05	none found	na
s43	m	HAEMATOPORPHYRIN	OG	OG	0	0	2	0	0.0E+00	34570963	Abeta42
s44	m	PROTOPORPHYRIN IX	OG	OG	0	7	2	6	2.1E-03	34570963	Abeta42
s45	m	CHLOROPHYLLIDE Cu COMPLEX Na SALT	OG	OG	0	0	2	0	0.0E+00	none found	na
s46	n	GOSSYPOL-ACETIC ACID COMPLEX	OG	OG	0	0	2	0	0.0E+00	none found	na
s47	n	GOSSYPOL	OG	OG	0	0	3	0	0.0E+00	21858698, 25043951, 32210536	IAPP
s48		DEMECLOCYCLINE HYDROCHLORIDE	OG	sick	0	6	2	9	4.4E-03	21068391, 28338670	β-2 microglobulin fibril
s49	r	DIHYDROCELASTROL	OG	OG	0	23	4	27	1.3E-03	none found	na
s50	r	CELASTROL	OG	OG	0	7	3	7	1.9E-05	none found	na
s51	o	ALIZARIN	OG	OG	0	13	2	6	2.3E-03	34033711	insulin fibrils
s52	o	PURPURIN	OG	OG	0	6	3	11	1.2E-04	34033711, 31562564	Insulin fibrils, Tau peptide
s53	p	GLICLAZIDE	OG	OG	0	0	2	0	0.0E+00	none found	na
s54	p	GLIMEPIRIDE	OG	OG	0	4	3	2	1.9E-07	none found	na
s55	p	GLIPIZIDE	OG	OG	0	28	2	9	8.3E-03	none found	na
s56	q	RAFOXANIDE	OG	OG	0	8	2	12	8.2E-03	none found	na
s57	q	CLOSANTEL	sick	sick	0	0	3	0	0.0E+00	none found	na
s58	q	OXYCLOZANIDE	OG	OG	0	27	4	30	2.6E-03	none found	na
s59		LEOIDIN	OG	OG	0	8	2	4	7.3E-04	US9463195B2	β-2 microglobulin
s60		TENIPOSIDE	OG	OG	0	27	2	0	1.7E-05	none found	na
s61		DIFFRACTAIC ACID	OG	OG	0	46	2	6	5.9E-03	none found	na
s62		BROMOCRIPTINE MESYLATE	OG	OG	0	0	2	0	0.0E+00	none found	na
s63		ADAPALENE	OG	OG	0	10	2	10	5.7E-03	28011763	Abeta42
s64		ERYTHROSINE SODIUM	OG	OG	0	4	3	3	1.1E-06	21354256, 28137461	lysozyme fibrils
s65		ITRACONAZOLE HYDROCHLORIDE	OG	sick	0	25	2	8	5.2E-03	none found	na
s66		NIFUROXAZIDE	OG	OG	0	24	4	32	3.1E-03	none found	na
s67		NITAZOXANIDE	OG	OG	0	3	3	6	8.4E-06	none found	na
s68		HARMALINE	OG	OG	0	36	2	1	4.4E-05	none found	na
s69		alpha-MANGOSTIN	OG	OG	0	0	3	0	0.0E+00	21958557; 28429536; 32419519	Abeta42; amyloidosis
s70		THIOSTREPTON	OG	OG	0	8	2	11	7.1E-03	none found	na
s71		APOMORPHINE HYDROCHLORIDE	OG	sick	0	25	2	1	1.3E-04	none found	na
s72		USNIC ACID	OG	OG	0	4	2	6	1.9E-03	none found	na
s73		BITHIONATE SODIUM	sick	sick	0	0	2	0	0.0E+00	none found	na
s74		CITRININ	OG	OG	0	13	4	26	4.9E-04	none found	na
s75		EBSELEN	OG	OG	0	21	2	6	3.3E-03	none found	na
s76		CANDESARTAN CILEXTIL	OG	OG	0	0	2	0	0.0E+00	none found	na
s77		TOTAROL	OG	OG	0	0	2	0	0.0E+00	none found	na
s78		CURCUMIN	OG	OG	0	3	3	4	2.9E-06	15590663, 17472706, 18189141 (lots)	Abeta42
s79		4,4'-DIMETHOXYDALBERGIONE	OG	OG	0	0	2	0	0.0E+00	none found	na
s80		DIHYDROGAMBOGIC ACID	OG	OG	0	12	2	8	4.0E-03	none found	na
s81		ISORESERPINE	OG	OG	0	6	2	1	9.0E-05	none found	na
s82		SAFROLE	OG	OG	0	12	2	16	1.7E-02	none found	na
s83		TRICLABENDAZOLE	OG	OG	0	20	4	28	1.3E-03	34547896	TTR amyloid
s84		ARIPIPRAZOLE	OG	sick	0	6	2	8	3.4E-03	none found	na
s85		SIROLIMUS	OG	OG	0	11	2	16	1.6E-02	none found	na

Supplemental Table 1. 85 Spectrum Suppressors of Small Molecule Crystallization in the Pharynx Cuticle.

[a]The node ID is the label of the node shown in Figure 4a.

[b]The cluster letter is that given to scaffold clusters shown in Figure 4a and 4b.

[c]The viability assay is the standard six day viability assay described in the methods. The number of replicates (n) is shown, and the mode is shown. OG, a culture overgrown with worms; sick, a culture with 11-50 worms; 0, a culture with 0-10 worms.

[d]The crystal formation assay is described in the methods section.

[e]The pubmed ID or patent number is shown that provides evidence for a primary role in fibril inhibition.

	Trivial Name	MolPort ID	Analog Smiles	Suppressor Analog[a]	48 hour crystal assay[b]			
					mean	n	sem	type
1	DMSO	negative control	na	na	0	6	0	-
2	wact-190	positive control	na	na	100	6	0	cry
3	RS-15	MolPort-001-814-824	c1cc2c(oc3ccc(cc3c2=O)Br)cc1	alpha-MANGOSTIN	100	4	0	cry
4	RS-50	MolPort-003-712-626	O=C1c2cc(ccc2C(=O)c2c1cccc2)F	PURPURIN/ALIZARIN	87	4	3	cry
5	RS-9	MolPort-002-211-224	O=C(c1ccc(OCC)cc1)c1ccc(cc1Cl)Cl	DDE	67	5	9	sph
6	RS-14	MolPort-000-690-079	c1(cc2c(oc3ccc(cc3c2=O)F)cc1)F	alpha-MANGOSTIN	66	4	12	cry
7	RS-11	MolPort-008-682-078	O=C(c1ccc(OCC)cc1)c1ccccc1Cl	DDE	60	3	19	sph
8	RS-40	MolPort-000-628-186	O=C1c2c(cccc2C(=O)c2c1cccc2)Cl	PURPURIN/ALIZARIN	56	5	7	cry
9	RS-6	MolPort-002-120-487	O=C(c1ccc(OC)cc1)c1ccc(cc1Cl)Cl	DDE	51	5	10	sph
10	RS-13	MolPort-001-814-873	O=C(c1ccc(cc1)F)C=Cc1c(cccc1)Cl	4'-HYDROXYCHALCONE	45	3	11	sph
11	RS-7	MolPort-002-120-597	O=C(c1ccc(OC)cc1)c1ccccc1Cl	DDE	41	3	10	sph
12	RS-41	MolPort-000-628-197	O=C1c2cccc(c2C(=O)c2c1cccc2Cl)Cl	PURPURIN/ALIZARIN	35	5	3	cry
13	RS-8	MolPort-002-209-464	O=C(c1ccc(OCC)cc1)c1ccc(cc1)Cl	DDE	26	5	6	cry
14	RS-10	MolPort-003-801-426	O=C(c1ccc(OC)c(c1)Cl)c1ccccc1	DDE	22	5	8	sph
15	RS-1	MolPort-000-153-180	O=C(c1ccc(OC)cc1)c1cccc(c1)Cl	DDE	14	5	7	sph
16	RS-46	MolPort-002-139-631	O=C1c2c(cccc2C(=O)c2c1cccc2)Br	PURPURIN/ALIZARIN	6	2	6	cry
17	RS-2	MolPort-000-153-182	O=C(c1ccc(OC)cc1)c1ccc(cc1)Cl	DDE	0	5	0	-
18	RS-5	MolPort-001-773-641	O=C(c1ccc(OC)cc1)c1ccc(cc1)F	DDE	0	4	0	-
19	RS-12	MolPort-009-323-013	O=C(c1ccc(OC)cc1Cl)c1ccccc1	DDE	0	5	0	-
20	RS-16	MolPort-000-153-368	O=C(Cc1ccccc1)c1ccc(cc1)Cl	ONONETIN	0	4	0	-
21	RS-18	MolPort-001-785-660	O=C(Cc1ccc(cc1)Cl)c1ccccc1	ONONETIN	0	4	0	-
22	RS-21	MolPort-002-498-703	O=C(Cc1ccc(c(c1)F)F)c1ccccc1	ONONETIN	0	4	0	-
23	RS-24	MolPort-003-899-970	O=C(Cc1ccc(cc1)F)c1ccc(cc1)Cl	ONONETIN	0	2	0	-
24	RS-26	MolPort-011-192-811	O=C(Cc1ccc(cc1)F)c1ccc(cc1Cl)Cl	ONONETIN	0	2	0	-
25	RS-27	MolPort-011-790-797	O=C(Cc1ccc(cc1Cl)Cl)c1ccc(cc1)Cl	ONONETIN	0	2	0	-
26	RS-28	MolPort-011-912-385	O=C(Cc1ccc(cc1)Cl)c1cccc(c1)F	ONONETIN	0	4	0	-
27	RS-29	MolPort-011-912-395	O=C(Cc1cccc(c1)F)c1cccc(c1)F	ONONETIN	0	4	0	-
28	RS-30	MolPort-011-912-620	O=C(Cc1ccc(cc1Cl)Cl)c1ccc(cc1)F	ONONETIN	0	4	0	-
29	RS-31	MolPort-012-334-336	O=C(Cc1ccc(cc1)Cl)c1ccc(cc1Cl)Cl	ONONETIN	0	2	0	-
30	RS-32	MolPort-013-275-146	O=C(Cc1cccc(c1)F)c1ccc(cc1)F	ONONETIN	0	4	0	-
31	RS-33	MolPort-013-289-535	O=C(Cc1cccc(c1)F)c1ccc(c(c1)Cl)Cl	ONONETIN	0	4	0	-
32	RS-38	MolPort-026-446-172	O=C(Cc1ccc(c(c1)F)F)c1ccc(cc1)Cl	ONONETIN	0	2	0	-
33	RS-45	MolPort-002-136-236	O=C1c2c(c(c(c(c2C(=O)c2c1cccc2)F)F)F)F	PURPURIN/ALIZARIN	0	2	0	-
34	RS-47	MolPort-002-250-630	O=C1c2c(c(c(c(c2C(=O)c2c1cccc2)Cl)Cl)Cl)Cl	PURPURIN/ALIZARIN	0	4	0	-
35	RS-48	MolPort-002-904-427	O=C1c2c(ccc(c2C(=O)c2c1cccc2)F)F	PURPURIN/ALIZARIN	0	4	0	-

Supplemental Table 2. Reduced Analogs of Suppressors.
Suppressors are listed in order of their ability to induced object formation.
[a]DDE, 3,4-DIDESMETHYL-5-DESHYDROXY-3'-ETHOXYSCLEROIN
[b]N, the number of trials (at least 20 animals were counted in each trial); SEM, standard error of the mean; type (of object) is either birefringent crystals (cry) or non-birefringent globular spheres (sph).

	Trivial Name	MolPort ID	Analog Smiles	Wactive Analog	6 day viability assay[a]						crystal counts[b]
					DMSO trial 1 (n=3)	DMSO trial 2 (n=3)	DMSO trial 3 (n=3)	w190 trial 1 (n=3)	w190 trial 2 (n=3)	w190 trial 3 (n=3)	w190 average +/- SEM (N=5, n>20)
1		DMSO (n=6)			OG	OG	OG	let	let	let	100 +/- 0
2	OC-1	MolPort-000-132-940	c1cc(c2nc(c3cccnc3)no2)c(cc1)O	wact-10-2	OG	OG	OG	let	let	let	
3	OC-2	MolPort-001-849-559	c1cccc(OCc2nc3ccccc3s2)c1O	wact-15	let	OG	OG	let	let	let	
4	OC-4	MolPort-000-369-009	c1ccccc1c1nnc(c2c(cccc2)O)o1	wact-51	OG	OG	OG	let	let	let	
5	OC-5	MolPort-000-156-303	O=C(c1ccccc1)Nc1cccc(c1)O	wact-128	OG	OG	OG	let	let	let	
6	OC-6	MolPort-000-516-315	O=C(c1ccccc1)Nc1ccc(cc1)O	wact-128	OG	OG	OG	let	let	let	
7	OC-7	MolPort-000-677-289	O=C(c1ccc(cc1)O)Nc1ccccc1	wact-128	OG	OG	OG	let	let	let	
8	OC-8	MolPort-001-011-775	O=C(c1ccccc1)Nc1ccccc1O	wact-128	OG	OG	OG	let	let	let	
9	OC-9	MolPort-001-781-621	O=C(c1c(cccc1)O)Nc1ccccc1	wact-128	OG	OG	OG	let	let	let	
10	OC-10	MolPort-001-783-472	O=C(c1c(cccc1)O)Nc1ccc(cc1)O	wact-128	OG	OG	OG	let	let	let	
11	OC-11	MolPort-002-323-598	O=C(c1ccc(cc1)O)Nc1ccc(cc1)O	wact-128	OG	OG	OG	OG	OG	OG	57 +/- 16 (p <0.3)
12	OC-12	MolPort-003-855-287	O=C(c1cc(ccc1)O)Nc1ccccc1	wact-128	OG	OG	OG	let	let	let	
13	OC-13	MolPort-046-069-921	O=C(c1ccccc1)Nc1ccc(cc1O)O	wact-128	OG	OG	OG	let	let	let	
14	OC-14	MolPort-008-388-876	c1cccc(c1c1nc(c2cccs2)no1)O	wact-169	OG	OG	OG	let	let	let	
15	OC-16	MolPort-001-900-048	c1cccc(c1c1nc(c2ccccc2)no1)O	wact-184	sick	OG	OG	let	let	let	
16	OC-17	MolPort-002-222-727	Brc1ccc(cc1)c1noc(c2ccc(cc2)O)n1	wact-184	OG	OG	OG	sick	OG	OG	0 +/- 0 (p =0)
17	OC-18	MolPort-000-519-488	c1ccccc1c1csc(Nc2cc(ccc2)O)n1	wact-393	sick	OG	OG	sted/dea	sick	let	
18	OC-20	MolPort-001-998-500	c1cc(c(cc1c1csc(Nc2ccccc2)n1)O)O	wact-393	OG	OG	OG	OG	OG	OG	46 +/- 17 (p <0.02)
19	OC-21	MolPort-001-998-519	c1cc(cc(c1c1csc(Nc2ccc(cc2)O)n1)O)O	wact-393	OG	OG	OG	sick	OG	OG	24 +/- 7 (p <0.001)
20	OC-22	MolPort-002-013-480	c1cc(ccc1c1csc(Nc2ccc(cc2)O)n1)O	wact-393	OG	OG	OG	sick	OG	OG	23 +/- 7 (p <0.001)
21	OC-23	MolPort-002-176-399	Br.Oc1ccc(Nc2nc(cs2)-c2ccccc2)cc1	wact-393	OG	OG	OG	let	let	let	
22	OC-24	MolPort-002-973-587	c1cccc(c1c1csc(Nc2ccccc2)n1)O	wact-393	OG	OG	OG	let	let	let	
23	OC-25	MolPort-001-945-190	O=C(Nc1ccc(c(c1)O)c1nc2ccccc2s1)c1ccccc1	wact-415	OG	OG	OG	let	let	sick	
24	OC-26	MolPort-001-945-191	O=C(c1c(cccc1)F)Nc1ccc(c(c1)O)c1nc2c(cccc2)s1	wact-415	sick	OG	OG	let	let	let	
25	OC-27	MolPort-003-180-443	c1ccccc1c1nnc(c2ccc(cc2)O)o1	wact-425	OG	OG	OG	let	let	let	
26	OC-29	MolPort-010-675-363	Clc1ccc(cc1)c1noc(c2c(nccc2)O)n1	wact-712-1	OG	OG	OG	let	let	let	

Supplemental Table 3. Halogenated Analogs of Crystal-Forming Molecules.

[a]OG, the majority of the wells in the trial were over-grown with more than 50 animals in each well; sick, the majority of the wells in the trial were sick with between 11 and 50 animals in each well; let, the majority of the wells in the trial had 10 or fewer animals.

[b]N is the number of trials; n is the number of animals counted in each trial; SEM is the standard error of the mean; the p value shown is from a Student's T-test between the experimental sample and the wact-190-only control.

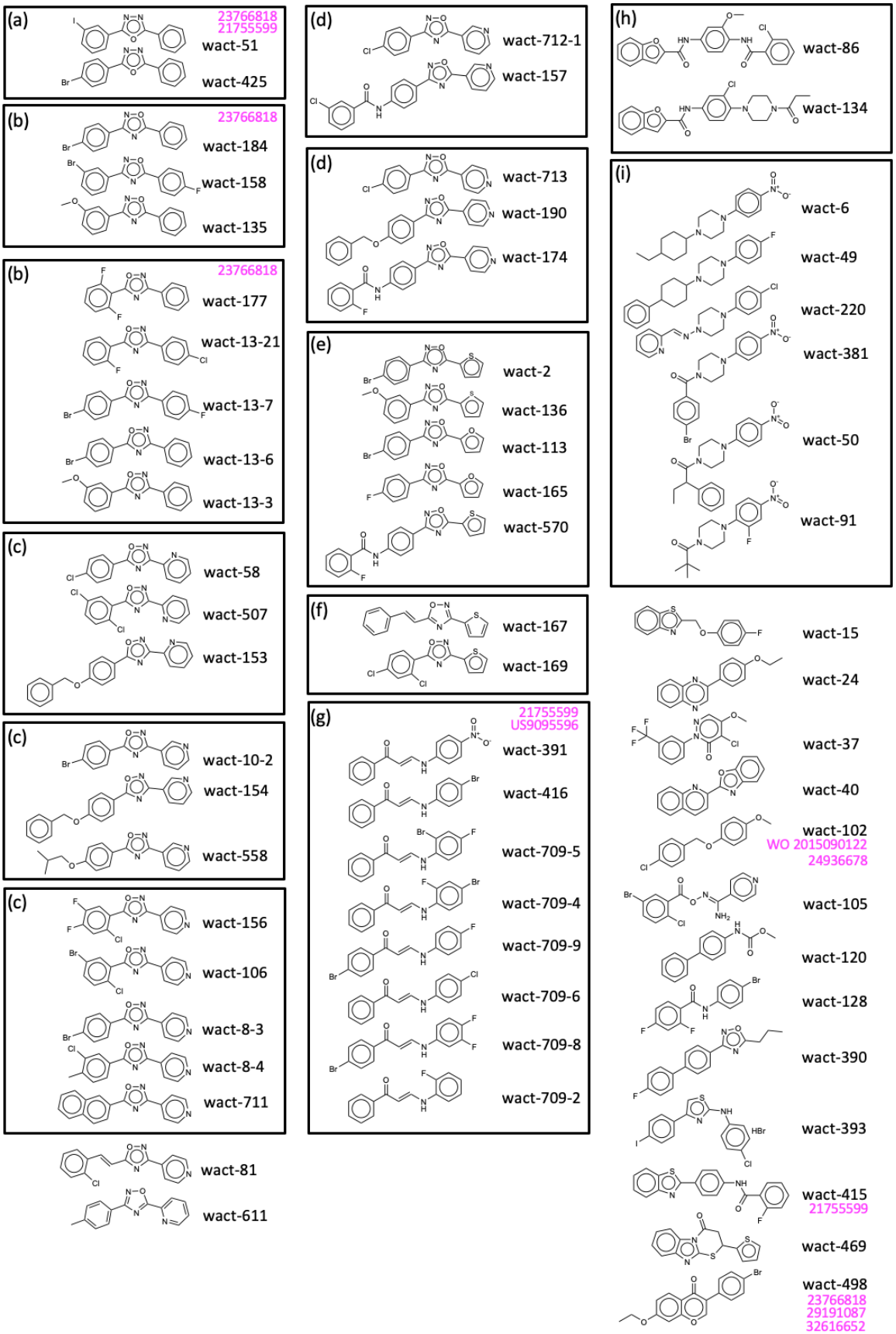
(a)
23766818
21755599
wact-51
wact-425
(b)
23766818
wact-184
wact-158
wact-135
(b)
23766818
wact-177
wact-13-21
wact-13-7
wact-13-6
wact-13-3
(c)
wact-58
wact-507
wact-153
(c)
wact-10-2
wact-154
wact-558
(c)
wact-156
wact-106
wact-8-3
wact-8-4
wact-711
wact-81
wact-611
(d)
wact-712-1
wact-157
(d)
wact-713
wact-190
wact-174
(e)
wact-2
wact-136
wact-113
wact-165
wact-570
(f)
wact-167
wact-169
(g)
21755599
US9095596
wact-391
wact-416
wact-709-5
wact-709-4
wact-709-9
wact-709-6
wact-709-8
wact-709-2
(h)
wact-86
wact-134
(i)
wact-6
wact-49
wact-220
wact-381
wact-50
wact-91
wact-15
wact-24
wact-37
wact-40
wact-102
WO 2015090122
24936678
wact-105
wact-120
wact-128
wact-390
wact-393
wact-415
21755599
wact-469
wact-498
23766818
29191087
32616652

922

923 **Supplemental Figure 1. Crystallizing Small Molecules Grouped According to Structural**
924 **Similarity.** Molecules belonging to structurally distinct families are boxed together. The
925 15 singletons are unboxed. The cluster that each boxed set of molecules belong to,
926 which corresponds to notation in Figure 1g, is indicated in the upper left-hand corner.
927 The pubmed IDs or patent numbers that provides evidence of binding to amyloid are
928 indicated in pink.

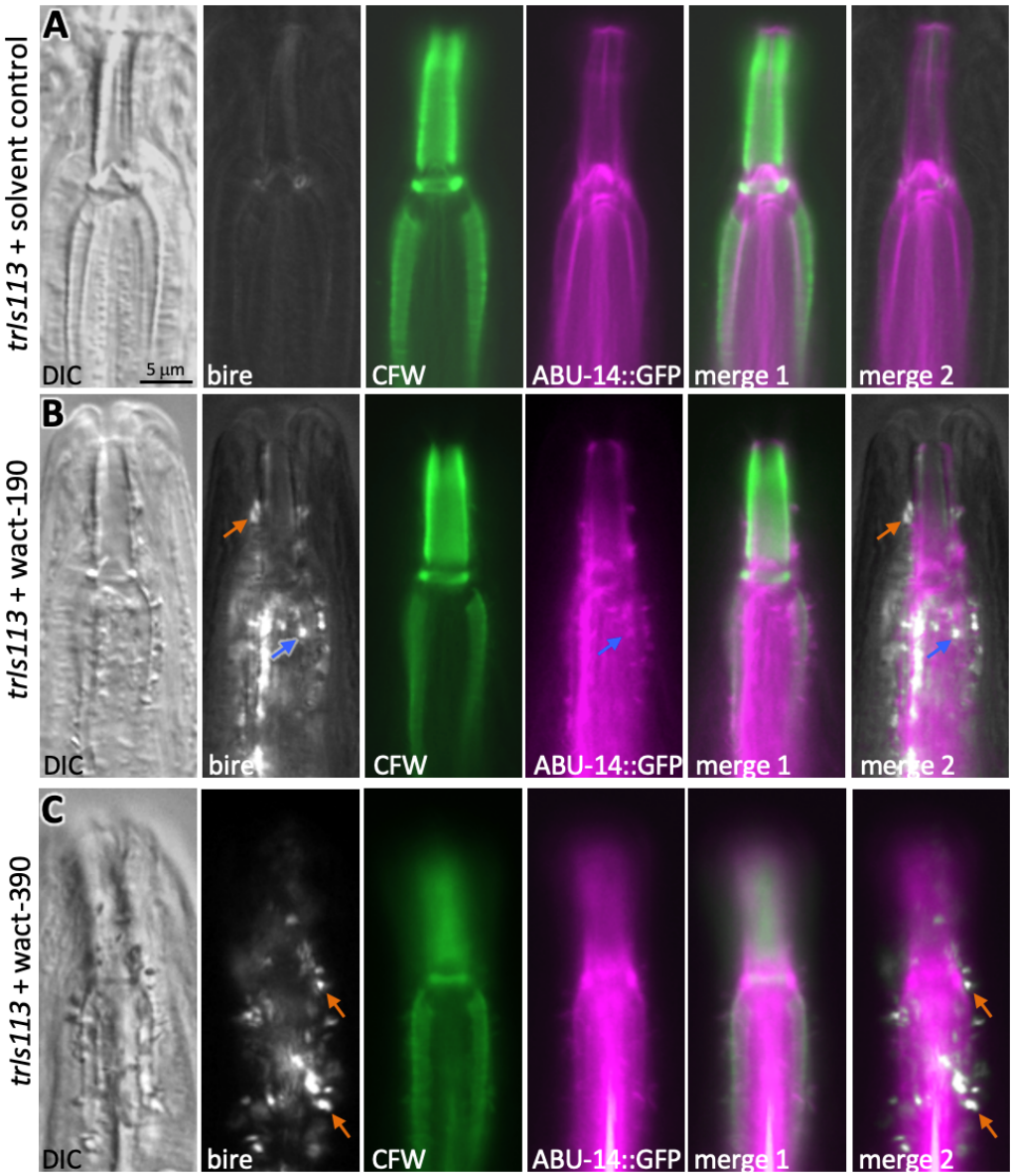

Supplemental Figure 2. Crystal-Induced Disruption of the ABU-14::sfGFP Pharyngeal Cuticle Marker. A-C. Images of animals expressing ABU-14::sfGFP (the extrachromosomal array, which we integrated as *trIs113*, was a kind gift from David Raizen) and stained with the indicated dyes. The imaging channel is indicated (lower left) as is the 3 hour wactive treatment (left-hand side of micrograph series). DIC, differential interference contrast; bire, birefringence; CFW, calcofluor white. Merge 1 is the merge of ABU-14::GFP and the CFW signal. Merge 2 is the merge of the signals from

940 ABU-14::GFP and the birefringence signal. Blue arrows indicate overlapping signals of
941 the amyloid-binding dye and birefringence; orange arrows show a lack of amyloid-
942 binding dye signal associated with birefringence signal. 60 μM of wact-190 and wact-390
943 was used in all experiments relevant to panels A-C.

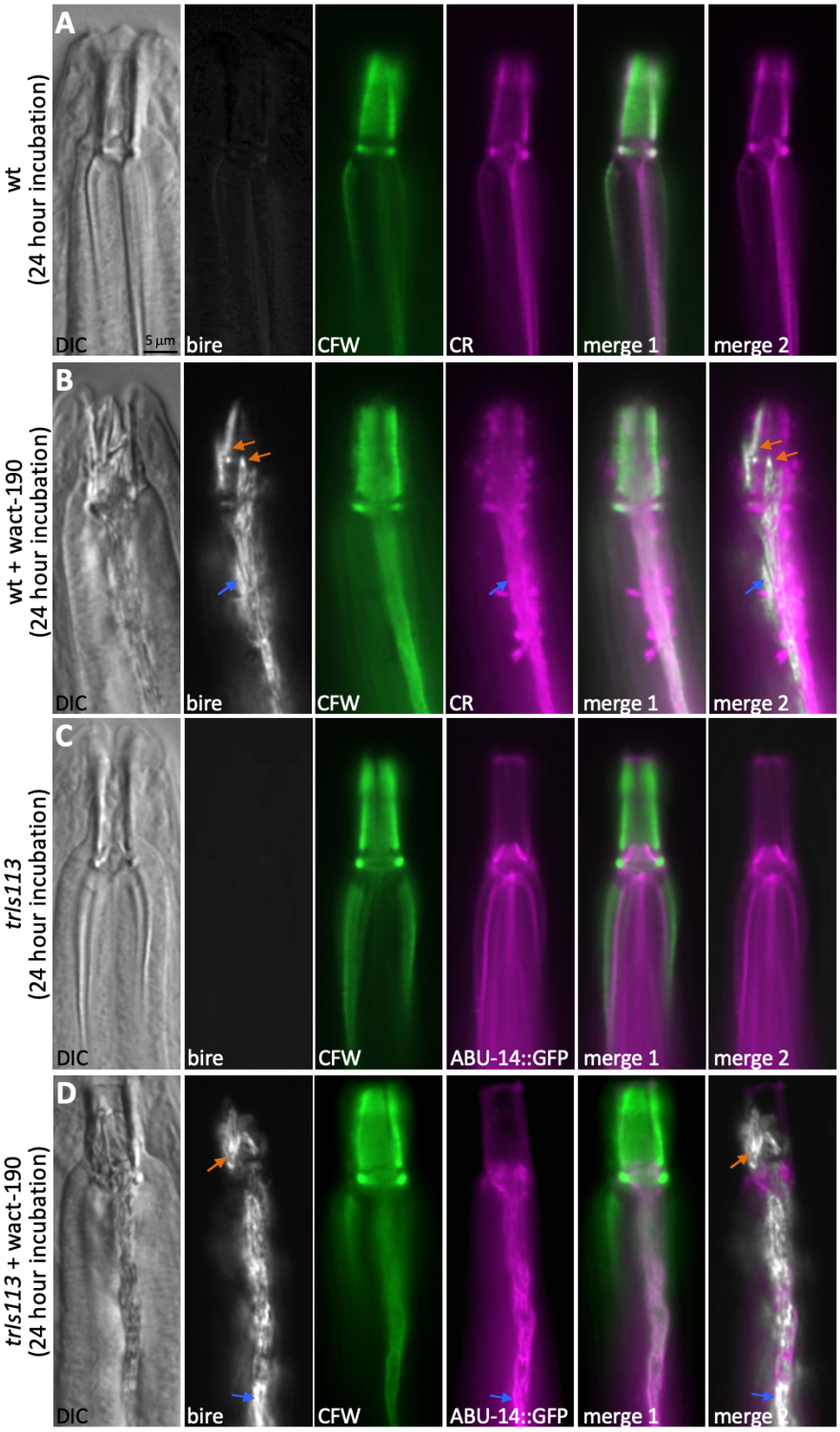

944 **Supplemental Figure 3. Larger wact-190 Crystals Often Fail to Overlap with Cuticle**

945 **Markers.** Legend is the same as that described for Figure 3 and Supplemental Figure 2.

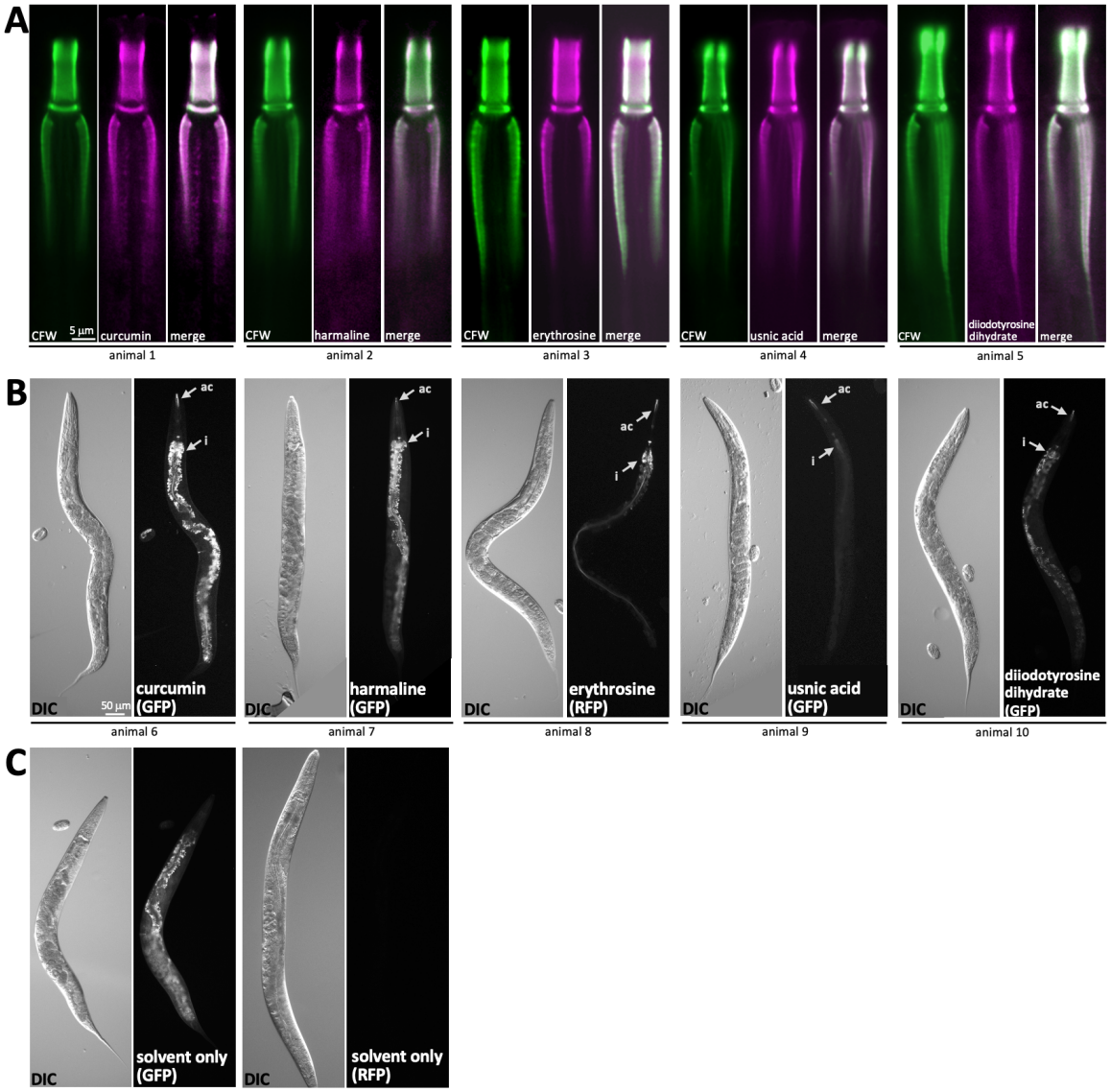

Supplemental Figure 4. Fluorescent Suppressors Specifically Localize to the Pharyngeal Cuticle. A. Calcofluor white (CFW) is used as counter-stain control for each of the molecules (60 µM) examined. **B-C.** B. Whole animal pictures illustrating the specificity of the localization of the indicated suppressor molecules. The intestine exhibits autofluorescence from gut granules, as illustrated in the no-dye control pictures (C). ac, anterior corpus; i, intestine.

A

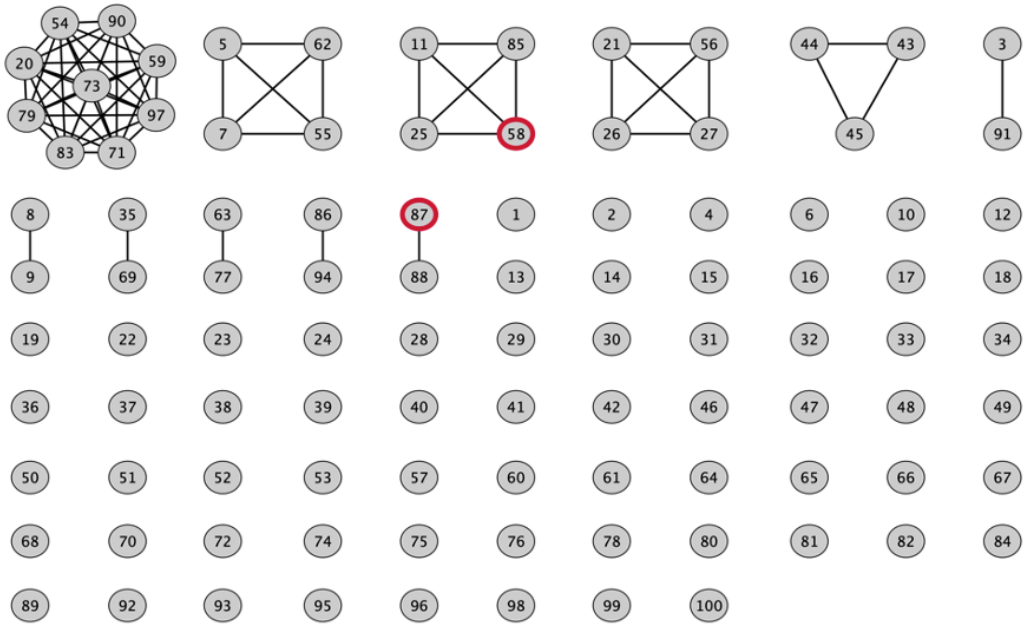

B

Node ID	Name of Molecule	Evidence for direct disruption of amyloid fibrils (PMID)	Targeted Amyloid
1	1,3-DIDEACETYL-7-DEACETOXY-7-OXOKHIVORIN	none	na
2	3-ACETAMIDOCOUMARIN	none	na
3	4,6-DIMETHOXYTOLUQUINONE	none	na
4	5-AMINOPENTANOIC ACID HYDROCHLORIDE	none	na
5	6,4'-DIMETHOXYFLAVONE	none	na
6	7-METHOXYCHROMONE	none	na
7	7,8-DIMETHOXYFLAVONE	none	na
8	8-HYDROXYCARAPINIC ACID	none	na
9	8beta-HYDROXYCARAPIN, 3,8-HEMIACETAL	none	na
10	ACETOHEXAMIDE	none	na
11	ACTINOQUINOL SODIUM	none	na
12	AMLEXANOX	none	na
13	ANAZOLENE SODIUM	none	na
14	ANDROGRAPHOLIDE	none	na
15	APRAMYCIN SULFATE	none	na
16	AVANAFIL	none	na
17	BEPHENIUM HYDROXYNAPTHOATE	none	na
18	BETULINIC ACID	none	na
19	BOLDINE	none	na
20	CAPOBENIC ACID	none	na
21	CARYOPHYLLENE [t(-)]	none	na
22	CEFAZOLIN SODIUM	none	na
23	CEFDINIR	none	na
24	CHLORPROTHIXENE HYDROCHLORIDE	none	na
25	CLOXYQUIN	none	na
26	CORTISONE	none	na
27	CRUSTECDYSONE	none	na
28	CYCLOPAMINE	none	na
29	CYCLOTHIAZIDE	none	na
30	CYPERMETHRIN	none	na
31	CYTISINE	none	na
32	DENATONIUM BENZOATE	none	na
33	DERRUSNIN	none	na
34	DIHYDROCELASTROL	none	na
35	DIPLOSALSALATE	none	na
36	DIRITHROMYCIN	none	na
37	DRONEDARONE HYDROCHLORIDE	none	na
38	EBASTINE	none	na
39	EBSELEN	none	na
40	ELLAGIC ACID	none	na
41	EPICATECHIN MONOGALLATE	none	na
42	ERGOTAMINE TARTRATE	none	na
43	ESTRADIOL ACETATE	none	na
44	ESTRADIOL-3-SULFATE, SODIUM SALT	none	na
45	ESTRAMUSTINE	none	na
46	ESTROPIPATE	none	na
47	ETHOXYQUIN	none	na
48	ETHOXZOLAMIDE	none	na
49	FENOLDOPAM MESYLATE	none	na
50	FENSPIRIDE HYDROCHLORIDE	none	na

Node ID	Name of Molecule	Evidence for direct disruption of amyloid fibrils (PMID)	Targeted Amyloid
51	FLAVANONE	none	na
52	FORMONONETIN	none	na
53	GLIQUIDONE	none	na
54	HALAZONE	none	na
55	HIERACIN	none	na
56	HYDROCORTISONE	none	na
57	IODIXANOL	none	na
58	IODOQUINOL	19664688	Abeta42
59	ISOBUTAMBEN	none	na
60	ISOGUVACINE HYDROCHLORIDE	none	na
61	IVERMECTIN	none	na
62	IZALPININ	none	na
63	LANSOPRAZOLE	none	na
64	LOVASTATIN	none	na
65	MEROGEDUNIN	none	na
66	MEROPENEM	none	na
67	METHAZOLAMIDE	none	na
68	METHYLPHENIDATE HYDROCHLORIDE	none	na
69	MONOBENZONE	none	na
70	MOROXYDINE HYDROCHLORIDE	none	na
71	N-METHYLBENZYLAMINE HYDROCHLORIDE	none	na
72	NATAMYCIN	none	na
73	OCTOPAMINE HYDROCHLORIDE	none	na
74	OLSALAZINE SODIUM	none	na
75	ORNIDAZOLE	none	na
76	PALMIDROL [5mM]	none	na
77	PANTOPRAZOLE	none	na
78	PHENYLBUTAZONE	none	na
79	PHENYLETHYL ALCOHOL	none	na
80	PODOFILOX	none	na
81	PREDNISOLONE SODIUM PHOSPHATE	none	na
82	PYRITHYLDIONE	none	na
83	PYROCATECHUIC ACID	none	na
84	QUINOLINIC ACID	none	na
85	SEROTONIN HYDROCHLORIDE	none	na
86	SHIKIMIC ACID	none	na
87	SULFAMETER	25043951	IAPP
88	SULFAMETHAZINE	none	na
89	TANSHINONE IIA SULFONATE SODIUM	none	na
90	THIMEROSAL	none	na
91	THYMOQUINONE	none	na
92	TILMICOSIN	none	na
93	TOLNAFTATE	none	na
94	TRETINOIN	none	na
95	TRICHLOROETHYLENE	none	na
96	TRIMEDLURE	none	na
97	TYROSINE HYDROCHLORIDE	none	na
98	URIDINE	none	na
99	VALSARTAN	none	na
100	VANITIOLIDE	none	na

952

953 **Supplemental Figure 5. The Construction and Analysis of a Random Network from the**
954 **Spectrum Library. A.** A structural similarity network of the 100 randomly chosen
955 Spectrum library molecules. The nodes (circles) represent a drug or natural product
956 whose number corresponds to the identity indicated in panel B. The links (straight lines)
957 represent a Tanimoto structural similarity coefficient of 0.8 or more (see methods). A
958 bold red outline indicates that the molecule is a known disruptors of amyloid fibril
959 formation (see panel B for details). **B.** The 100 molecules randomly chosen from the
960 Spectrum Library that were used the build the network depicted in panel A. The node ID
961 is the label of the node shown in panel A. The pubmed ID is shown for those molecules
962 for which evidence could be found of a primary role in fibril inhibition.

963 **Supplementary Data File 1.**

964 The 'RL1200' library and associated screening data that revealed 16 additional

965 crystalizing molecules. See methods and main text for details. Red cells on the table

966 indicate that the culture is dead (fewer than 12 animals remaining); orange and yellow

967 indicate that the culture is sick (between 12 and 50 animals), and green indicate that the

968 culture is growing well. OG, over-grown; L, larvae; A, adults.